Exploring aerosols near clouds with high-spatial-resolution aircraft remote sensing during SEAC^{4}RS

Robert S. Spencer[1,2, †], Robert C. Levy[2], Lorraine A. Remer[4], Shana Mattoo[1,2], George T. Arnold[1,2], Dennis L. Hlavka[1,2], Kerry G. Meyer[2], Alexander Marshak[2], Eric M. Wilcox[3] and Steven E. Platnick[2]

[1] Science Systems and Applications, Inc, Lanham, Maryland, USA.

[2] Laboratory for Atmospheres, NASA Goddard Space Flight Center, Greenbelt, MD, USA.

[3] Division of Atmospheric Sciences, Desert Research Institute, Reno, NV, USA

[4] Joint Center for Earth systems Technology (JCET), University of Maryland Baltimore County, Baltimore, MD USA

†Now at: National Renewable Energy Laboratory (NREL), Golden, CO USA

Corresponding author: Robert Levy (robert.c.levy@nasa.gov)

Key Points:

- An aerosol retrieval algorithm is ported from a satellite sensor to a higher-spatial resolution aircraft sensor.
- The retrieval is applied and compared with other datasets from a 2013 airborne field campaign over the southeastern U.S.
- Comparative data suggests that retrievals of enhanced aerosol optical depth (AOD) near clouds is primarily an adjacency effect.

Plain Language Summary

Since aerosols are important components of our climate system, we seek to use observations to quantify aerosol properties and their interactions with clouds. To study aerosols close to clouds, we adapt a well-known aerosol retrieval algorithm used for satellite remote sensing (lower spatial resolution) and port to airborne remote sensing (higher spatial resolution). We apply the retrieval to observations collected over the southeastern United States during late summer 2013. The resulting product suggests that total aerosol optical depth (AOD) can be greatly enhanced near clouds. To validate, we compare this retrieved AOD to other datasets, and find that the enhanced AOD near clouds is only partially observed by other sensors. This suggests that the enhanced AOD is primarily a cloud adjacency, or 3-dimensional radiative effect. High-resolution, passive remote sensing measurements can characterize aerosol/cloud environments, thus helping to interpret global AOD datasets from more comprehensive, but coarser-resolution satellite retrievals.

Abstract

Since aerosols are important to our climate system, we seek to observe the variability of aerosol properties within cloud systems. When applied to the satellite-borne Moderate-resolution Imaging Spectroradiometer (MODIS), the Dark Target (DT) retrieval algorithm provides global aerosol optical depth (AOD at 0.55 μm) in cloud-free scenes. Since MODIS' resolution (500 m pixels, 3 km or 10 km product) is too coarse for studying near-cloud aerosol, we ported the DT algorithm to the high-resolution (~50 m pixels) enhanced-MODIS Airborne Simulator (eMAS), which flew on the high-altitude ER-2 during the Studies of Emissions, Atmospheric Composition, Clouds and Climate Coupling by Regional Surveys ($SEAC^4RS$) Airborne Science Campaign over the U.S. in 2013. We find that even with aggressive cloud screening, the ~0.5 km eMAS retrievals show enhanced AOD, especially within 6 km of a detected cloud. To determine the cause of the enhanced AOD, we analyze additional eMAS products (cloud retrievals and degraded-resolution AOD), co-registered Cloud Physics Lidar (CPL) profiles, MODIS aerosol retrievals, and ground-based Aerosol Robotic Network (AERONET) observations. We also define spatial metrics to indicate local cloud distributions near each retrieval, and then separate into near-cloud and far-from-cloud environments. The comparisons show that low cloud masking is robust, and unscreened thin cirrus would have only a small impact on retrieved AOD. Some of the enhancement is consistent with clear-cloud transition zone microphysics such as aerosol swelling. However, 3D radiation interaction between clouds and the surrounding clear air appears to be the primary cause of the high AOD near clouds.

1 Introduction

Aerosols are important components of the climate system, acting directly to scatter sunlight back to space and indirectly by modifying cloud microphysical and macrophysical properties (Boucher et al., 2013). Changes in aerosol loading and properties (e.g. size and shape distribution) lead to changes in both the microphysical properties and the radiative distribution of the cloud field (Koren et al., 2009). Additionally, aerosols impact the formation, reflectivity, and behaviors of clouds, leading to indirect effects on radiative forcing, modifications to cloud development and effects on precipitation (Muhlbauer and Lohmann, 2009; Zhang et al., 2016). To answer fundamental questions about our changing climate, we must quantify current aerosol properties and their interactions with clouds (Rosenfeld et al., 2014; Seinfeld et al., 2016). While quantifying these properties through observations is difficult at any scale, it is particularly challenging to observe Aerosol-Cloud-Interactions (ACI) at global and climate-relevant scales.

Passive satellite remote sensing is a vital tool for characterizing the global distribution of aerosol properties in cloud-free skies. In particular, the Moderate Imaging Spectroradiometer (MODIS) Dark Target (DT) algorithm has generated datasets of aerosol optical depth (AOD) and other aerosol parameters since the launch of Terra in 1999 (Remer et al., 2005). The issue, however, is that aerosol properties are only retrieved in clear-sky conditions. A pixel must be identified as cloud-free and appropriate for an aerosol retrieval (Remer et al., 2012; Levy et al., 2013). The "cloud mask" designed for aerosol retrieval must minimize sub-pixel cloud (and other) contamination (Zhang et al., 2005) while maximizing retrieval availability (Remer et al., 2012). Since clouds tend to be brighter, cooler, and more spatially heterogeneous than aerosols or the surface below (Stubenrauch et al., 2009), the DT strategy is to combine tests using absolute values of reflectance (in both visible-wavelength "window" and shortwave-infrared water-absorption "cirrus" bands), absolute values of infrared-derived temperature, and standard deviation upon 3x3 pixel aggregations (Martins et al., 2002; Gao et al., 2002).

Achieving a balance between minimizing data contamination and maximizing its availability is inherently challenging. For one, there is the problem of thin cirrus that may not be detected by either infrared temperature or water-absorption cloud masks (Dessler and Yang, 2003; Kaufman et al., 2005; Ackerman et al., 2008). There is also a transition zone from liquid clouds to clear sky, termed the "twilight zone" or the “continuum” (Charlson et al., 2007; Koren et al. 2007). This zone is characterized by increased humidity near clouds that causes aerosol particles to become more hydrated and swell in size. The result is ambiguous optical properties and increased AOD (Quaas et al. 2010). At the same time this zone is filled with evaporating cloud droplets that are becoming smaller in size, and cloud fragments that add to the confusion.

Clouds are also sources of aerosols, generating new particles through aqueous chemistry and subsequent evaporation. These cloud-processed particles add to the AOD adjacent to clouds (e.g., Marshak et al., 2008; Tackett and diGirolamo, 2009; Varnai and Marshak, 2009, 2012; Chand et al., 2012; Eck et al., 2014; J. Wang et al., 2016; Varnai et al., 2017), and may have very different optical properties than those particles initially available to seed the cloud (Hoppel et al., 1986). From a remote sensing standpoint, the transition zone inhibits our ability to distinguish cloud-free from cloudy pixels. More importantly, the transition zone is not necessarily an artifact, and instead contributes to Earth’s albedo. According to Rosenfeld et al. (2014) and Seinfeld et al. (2016), the processes within this zone are not represented within current satellite retrieval products.

In addition to the complexity of the near-cloud physical environment, cloud adjacency effects, sometimes called 3D effects, cause the area surrounding clouds to appear brighter to imaging sensors flying above. Radiation is scattered from clouds into the areas that would be classified as cloud-free, and from there scattered by particles and molecules into the sensor’s field of view. This leads to increases in observed reflectance. According to Várnai and Marshak (2009, 2012, 2014), this 3D radiative process significantly contributes to near-cloud enhancement of observed reflectance, leading to retrieval of high-biased AOD. Although efforts have been made to correct AOD data products for these cloud effects (Wen et al., 2013; Marshak et al., 2008, 2014), they are not yet included within the aerosol retrieval algorithm.

A third reason for enhanced AOD near clouds is pure artifact of a sensor’s pixel point spread function or response time in its scan across the swath. There can be a “smearing” of detector response as the scan moves from a bright target to a darker target so that the darker target is artificially registering photons that should belong to the brighter target (Varnai and Marshak, 2009). The aerosol algorithm will interpret those additional photons as scattering from aerosol and artificially increase the AOD.

It is likely that the transition zone, 3D radiative processes and sensor response effects enhance AOD differently, at different distances from the cloud (e.g. Várnai and Marshak, 2018). The sensor response and cloud adjacency effects are expected to dominate close to cloud, while the transition zone effects (cloud environment) may extend 10 to 30 km away (Bar-Or et al., 2010). MODIS product resolutions are inherently too coarse to unravel the relative importance of transition zone, adjacency and detector effects, nor to properly characterize the mix of hydrated aerosol and evaporating cloud droplets in the transition zone. The coarse resolution cannot determine the gradient of aerosol properties in a near-cloud scene, much less the radiative forcing of these scenes. Therefore, to improve our knowledge of the near-cloud environment from a remote sensing perspective, we must use higher resolution data.

In particular, the MODIS Airborne Simulator (MAS), when flown on NASA's high-altitude ER-2 platform (~20 km altitude), offers an opportunity to observe like MODIS, but with ~50 m pixel resolution. Thus, we can explore gradients and conditions near clouds. Here, we port the (Collection 6) MODIS dark-target algorithm (DT) to enhanced-MAS (eMAS) data generated during NASA's SEAC^{4}RS Airborne Science Campaign. In section 2, we describe the DT algorithm as applied to MODIS sensors and how it is ported to MAS in general. In section 3, we introduce the SEAC^{4}RS experiment, the specific configuration of eMAS, as well as other datasets that will be used in the analysis. Section 4 illustrates the high-resolution eMAS aerosol imagery with three case studies. Section 5 evaluates the eMAS data as compared to MODIS and AERONET. Section 6 looks at the eMAS-generated AOD near clouds. This includes the creation of spatial metrics to explore near cloud observations as well as to compare with collocated Cloud Physics Lidar (CPL). Finally, Section 7 summarizes these findings and links to the eMAS AOD data products.

2 MODIS, eMAS and the dark-target retrieval algorithm

2.1 MODIS and DT aerosol retrieval

MODIS observes radiant energy at the top-of-atmosphere (TOA) in 36 wavelength bands (0.41 – 14.2 μm), and a variety of disciplines (land, ocean, atmosphere, cryosphere, etc.) use these data to create suites of products describing a wide array of geophysical parameters, diagnostics and quality indicators. In this study, we use the Level 2 (L2) Atmosphere products (http://modis-atmosphere.gsfc.nasa.gov) from Collection 6 (C6). These include a standard MODIS cloud mask (MxD35; Frey et al., 2008; Ackerman et al., 2010), cloud optical properties (MxD06; Platnick et al., 2017), and aerosol properties (MxD04) where MxD refers to either MOD or MYD depending on whether derived from MODIS-Terra or MODIS-Aqua. The MxD35 cloud mask estimates the presence/absence of clouds at 1 km resolution, using 36 tests involving all wavelength bands, and is used as input for deriving both cloud and aerosol properties. The aerosol product (MxD04) includes MxD04_L2 derived at nominal spatial resolution of 10 km (Hsu et al., 2013; Levy et al., 2013; Sayer et al., 2013) and MxD04_3K, derived at 3 km (Remer et al., 2013).

The MODIS C6 aerosol products represent the intersection of three retrieval algorithms (Hsu et al., 2013; Levy et al., 2013; Sayer et al., 2014). Two of the three are denoted as "dark-target" (DT) because they are optimized over surfaces that appear "dark" to our eyes. This includes open ocean water (DT-O) and vegetated/dark soiled land (DT-L). The third is the Deep Blue (DB) (Hsu et al., 2013) algorithm which was initially optimized over bright deserts that appear bright and uses Deep Blue wavelength bands (e.g. 0.41 μm). Here we focus on the DT retrieval.

The DT algorithms aggregate pixels into a standard 10 km (MxD04_L2) product, NxN means 10x10 of the 1 km pixels and 20x20 of the 500 m pixels. For the newer 3 km product (MxD04_3K), NxN is 3x3 and 6x6, respectively. Once aggregated, there are many tests that filter/discard inappropriate pixels from the retrieval box. Primarily these discarded pixels are associated with clouds, but they could also be associated with surface properties that lie outside algorithm assumptions. Many tests are used to find and discard cloudy pixels, including: (a) a subset of tests provided by the standard MODIS cloud mask, (b) additional tests that analyze the spatial variability within 3x3 pixel groupings (Martins et al., 2002), and (c) specific cirrus-confronting tests based on the 1.38 µm band (Gao et al., 2002). Additional tests using a variety of thermal emissive bands (TEB) and reflective solar bands (RSB) help remove ocean pixels with high sediment loadings (Li et al., 2003), pixels that appear to be ice or snow (Li et al., 2005), or pixels that appear to be deserts, or otherwise too bright to be dark-targets. Pixels that appear to contain subpixel water are also discarded from land aggregations.

Once all non-suitable pixels are discarded, there are statistical tests to discard outliers. To complete the input manipulation, DT corrects for absorption by gases (Patadia et al., 2018), relying on the NCEP estimates of water vapor and ozone columns. After all tests and corrections are performed, the remaining pixels (within the NxN box) are averaged, which becomes the input spectral reflectance (in seven bands) used for the DT retrieval. The DT algorithm over ocean returns spectral AOD and information on particle size including Angstrom Exponent. However, over land the DT algorithm is limited by the uncertainty in characterizing the surface reflectance and returns only AOD. Flowcharts and details for the DT retrieval over both ocean and land surfaces can be found in the literature (Remer et al., 2005; Levy et al., 2007a; Levy et al., 2013) and online (e.g. https://darktarget.gsfc.nasa.gov).

The standard MODIS DT retrieval produces a robust aerosol product, well-validated, and with minimal cloud contamination. However, to minimize the latter and achieve a high level of accuracy, the DT algorithm employs an aggressive cloud masking scheme, losing availability near and within cloud fields. The resolution (~10 km) does not permit resolving aerosol conditions close to clouds. This creates a clear-sky bias in regional and global characterization of mean aerosol characteristics (e.g. Zhang and Reid, 2009). Because global cloud fraction is ~70-75% (Stubenrauch et al., 2009; Mace and Zhang, 2014), there is a significant uncertainty in quantifying the global aerosol effect from these clear-sky biased statistics.

2.2 MAS/eMAS

With ~500 m -1.0 km native pixel resolution, and 3-10 km retrieval resolution, MODIS does not have the ability to characterize aerosol within highly variable cloud fields. Therefore, we look toward a higher-resolution dataset to explore these conditions.

Prior to the launch of Terra in 1999, the MODIS Airborne Simulator (MAS; King et al., 1996) was developed to support algorithm development and validation. Having a similar wavelength range as MODIS (0.47 through 14.2 µm), MAS simulates space-borne MODIS observations by flying at high-altitude (nominally 20 km) on NASA's ER-2 aircraft. Since the ER-2 at ~20 km is above 95% of the earth's atmosphere (above the troposphere), and by viewing with 2 mrad angular resolution, MAS pixel spatial resolution is approximately 50 m x 50 m at nadir. As MAS is designed to oversample and ensure no gaps between pixels, along-track pixel center distances tend to be slightly smaller (e.g. ~40 m).

Since the mid-1990s, MAS has flown in support of many diverse field experiments (http://mas.arc.nasa.gov/campaigns.html). Recently, the MAS scanner was retrofitted with an upgraded thermal-infrared spectrometer and is now referred to as the enhanced-MAS (eMAS). The eMAS instrument is maintained and operated by the Airborne Sensor Facility at NASA Ames Research Center in Mountain View, California, under the oversight of the EOS Project Science Office at NASA Goddard. The eMAS-observed swath is 710 pixels across, producing imagery on-ground with a width of ~37.5 km. eMAS data are organized by ER-2 flight and then separated into segments known as flight tracks. Although there are ER-2 flight tracks that dip or spiral, we are interested in flight tracks which are along near-constant altitude and headings. The length of flight tracks varies from ~50 km to ~1000 km.

MAS/eMAS uses two focal 'ports' for RSBs, one for observing VIS-NIR (λ<1.0 μm), the second for observing SWIR (between 1.6 – 2.5 μm). A third port is used for Mid-infrared (MIR; ~3 – 4 μm), and a fourth for observing Thermal-IR (TIR>6 μm). Whether MAS or eMAS, the first 25 channels are RSBs (port 1 and port 2). For MAS, there were 25 channels between MIR and TIR (making 50 total channels), but there are only 13 as eMAS (38 total). The RSB setup uses a grating spectrometer that can be shifted right or left to fine-tune the wavelength bands. Sometimes these shifts are intentional, but other times they are due to the experience of rough conditions (ER-2 flights themselves, integration/de-integration, transport, storage, etc.). Nonetheless, regular characterization of spectral response functions (SRF) shows that wavelength bands tend to stay centered within about ±0.02 μm of most analogues on MODIS (http://mas.arc.nasa.gov/). King et al. (1996) provide many more details of MAS optics, mechanics and data collection.

Organized by flight and flight track, Level 1B (L1B; calibrated reflectance/radiance known as MASL1B or eMASL1B) and Level 2 (L2) cloud products (MASL2CLD or eMASL2CLD – similar to MxD06) for many previous field experiments are available via the LAADS website. Imagery for these data are accessed via NASA-Langley's MAS website (https://mas.arc.nasa.gov/). Although not publicly archived, there is also a MxD35-like cloud mask for MAS (King et al., 2004; Ackerman et al., 2010; King et al., 2010).

2.3 DT algorithm for MAS

Porting the modern MODIS DT algorithm to another sensor presents specific challenges (Levy et al., 2015). We note that the original MODIS DT algorithms were first formulated to run on MAS data, which provided the test bed for MODIS algorithm development (Kaufman et al., 1997, 1998; Tanré et al., 1999). However, since 2000, there has been no MODIS-like aerosol retrieval performed on MAS or eMAS imagery.

The MAS (or eMAS) RSB spectral configuration is very close to that of MODIS. MAS/eMAS and MODIS both provide measurements near 0.47, 0.55, 0.65, 0.86, 1.63 and 2.11 μm (e.g., MODIS B1-4, B6 and B7). There is a gap between 1.0 and 1.6 μm, which means there is no equivalent 1.24 μm (B5) nor 1.38 μm (B26) on eMAS. eMAS, however, provides observations in many bands between 1.61 and 2.37 μm (approximately 0.05 μm interval) compared to only two from MODIS. This range includes the H_2O-absorbing 1.88 μm band. According to Gao et al. (2004) and Meyer et al. (2016), the 1.88 μm channel can be substituted (and is an improvement) for the 1.38 μm channel for cirrus detection. The remaining challenge is the missing 1.24 μm band, which is used by the MODIS DT algorithm to mask for snow/ice (Li et al., 2005), mask sediments in the ocean (Li et al., 2003), and to help identify dark-target surface reflectance over land (Levy et al., 2007b). For the study presented here, the SEAC4RS campaign in the summer over North America, the loss of snow/ice masking is unimportant. Meanwhile, ocean sediment masking is still adequate if only one of the 1.24 or the 1.63 μm bands is available, and substitutes for 1.24 μm can be found using other channels to characterize dark vegetated surfaces (Karnieli et al., 2001), including the traditional NDVI computed from 0.65 and 0.86 μm.

This means that other than the missing 1.24 μm band, the DT algorithm can be applied to MAS data almost exactly as to MODIS. However, new LUTs need to be created that correspond to the sensor response function (SRF) (Levy et al., 2015) measured during the particular MAS/eMAS campaign. These are calculated using the same methods and radiative transfer codes used by the MODIS algorithm (Ahmad and Fraser, 1982; Levy et al., 2015), also accounting for differences in gas absorptions cause by the new SRFs (Patadia et al., 2018).

Mechanically, our MAS retrieval follows that of MODIS. However, instead of NxN aggregations of native 500 m pixels becoming 10 km (or 3 km) spatial resolution retrievals, we choose 10x10 aggregations of MASL1B to become ~0.5 km retrievals. While probably too crude near coastlines, we use the same 0.25 km land/water mask (Carroll et al., 2016) and the same ancillary inputs (ozone, water vapor, wind speed) as MODIS. Cloud detection/masking for our MAS retrieval generally follows the same logic as does for MODIS, though in some cases using different wavelengths. For cirrus detection, the MODIS 1.38 μm threshold values for reflectance (cloudy if absolute > 0.025) are applied to 1.88 μm. The MAS-DT algorithm also has available a MxD35-like cloud mask, but applied to eMAS data, so that it can use the same cloud mask tests as it does for MODIS.

Another option for performing an eMAS aerosol retrieval is to first degrade the reflectances from 50 m to 500 m, and then perform retrievals to provide a ~5 km aerosol product. This can be used to compare with MODIS at its native resolution.

The MODIS DT retrieval code had been previously "modularized" for use on VIIRS or other sensors (Levy et al., 2015), and this version is applied here. Retrieved AOD, FMW and most diagnostics products can be similar to those provided with standard MxD04_L2 outputs. Nearly all tests in determining Quality Assurance and Confidence (QAC) are similar to the MODIS retrieval. One exception is on assigning QAC based on the number of pixels available out of the NxN. For MODIS (20x20 pixels at 0.5 km), QAC=3 (best confidence) over land requires 10% of the NxN. We choose to use the same % in defining QAC for the 10x10 box for MAS. The final aerosol product is nominally ~0.5 km spatial resolution (at nadir), having 71 pixels across-swath, and varying length along-track. The degraded resolution (~5 km) has only 7 pixels across track.

3 SEAC^{4}RS data sets

3.1 SEAC^{4}RS

During August and September of 2013, NASA conducted the Studies of Emissions, Atmospheric Composition, Clouds and Climate Coupling by Regional Surveys (SEAC^{4}RS) Airborne Science Campaign over the U.S. (Toon et al., 2016). The campaign included the NASA ER-2 aircraft carrying multiple sensors, including eMAS and the Cloud Physics Lidar (CPL; McGill et al., 2002). Flights covered much of the continental United States. Details of flights and graphics of flight paths for the entirety of the deployment are presented in Toon et al. (2016).

Ground-based support included deployment of multiple AERONET sites, which are also used here to evaluate eMAS retrievals. Finally, there were a number of MODIS (both Terra and Aqua) and VIIRS (on Suomi-NPP) overpasses that were at least partially collocated with the eMAS flight tracks.

3.2 eMAS products, including DT aerosol retrieval

During SEAC^{4}RS, there were 19 flights of the ER-2, organized into 376 eMAS flight tracks. The eMASL1B and the eMASL2CLD data are already available at the NASA LAADS website (http://mas.arc.nasa.gov/data/deploy_html/seac4rs_home.html). We note that the nominal altitude of the ER-2 during SEAC4RS ranged between 18-19 km (instead of 20 km), leading to native pixel spatial resolutions of ~ 46 m. Due to oversampling, the distance between pixel centers is 35-40 m (at nadir, along-track). To avoid confusion, we continue to refer to pixel size/retrieval size as 50 m/0.5 km, unless necessary to discuss otherwise. When discussing degraded resolution retrievals, pixel/retrieval sizes are 500 m/5 km.

The sensor response function (SRF) center-band wavelengths typically vary by ±0.02 μm from campaign to campaign. During SEAC4RS, the RSBs were mostly centered within ±0.01 μm of MODIS analogues (Table 1). We created LUTs for these wavelengths, and gas absorption correction formulas (e.g. Levy et al., 2015) for the specific SEAC4RS SRF.

*Table 1 List of DT wavelength bands for MODIS and their MAS equivalents. Centroid wavelengths are listed for MODIS (second column), for eMAS during SEAC4RS (third column). *The MODIS 1.38 μm "cirrus" channel is replaced by 1.88 μm on MAS.*

MODIS Band #	**Central MODIS Wavelength (μm)**	**Central Wavelength for SEAC^{4}RS eMAS (μm)**
3	0.466	0.467
4	0.554	0.550
1	0.645	0.655
2	0.855	0.864
3	1.238	N/A
4	1.628	1.605
5	2.113	2.125
26	1.380*	1.877*

Using the archived eMASL1B data, and applying both the MODIS-like cloud mask and the aerosol spatial variability masks, we performed the aerosol retrieval (described in Section 2.3) on all flight tracks. Note that these retrievals were made regardless of whether they were sufficiently near-constant in altitude and heading. We have made the 0.5 km product publicly available as 'eMASL2AER' data also at LAADS. Like MODIS, we have provided the data in HDF4 format, organized into Scientific Data Sets (SDSs). While not every MxD04_L2 SDS has an analogue here, most of the DT-related ones (Levy et al., 2013) are included. One exception is that only the "average" solution (and not the "best" solution) for ocean retrieval is provided. Following MODIS C6, we provide the DT cloud mask, or "Aerosol_Cldmask_Land_Ocean" which is a binary indicator of cloud/no cloud at native pixel resolution. New eMASL2AER SDSs include "Aircraft_Altitude" (altitude along-track), and an integer-based "Error_Flag_Land_And_Ocean". SEAC^{4}RS Level 2 cloud and aerosol products are publicly available at https://modis-images.gsfc.nasa.gov/SEAC4RS/emas/emas_seac4rs_L2_imagery.html. Note that only non-degraded eMASAER products are archived at LAADS.

Fig. 1 presents an example retrieval for flight (#13_959) track segment #10 (20:00-20:09) over Kentucky on 30 August. On the left side (panels A, B and C) we plot the true color RGB (at 50 m), the DT cloud mask (at 50 m) and the retrieved AOD (at 500 m). The DT cloud mask is the final result of combining the standard MODIS-like cloud mask ingested as an input to the algorithm with the internal tests (absolute and spatial variability) performed within the algorithm. On the right side, we plot the DT cloud mask (500 m) and retrieved AOD (at 5 km) corresponding to degraded eMAS spatial resolution.

From visual inspection and comparison of the RGB "true color" image with the results of the high-resolution cloud mask, it appears that the cloud mask successfully identifies the small cumulus clouds that cover the scene and that the aerosol algorithm is retrieving from the cloud-free pixels. The cloud mask also appears successful at discarding obvious cloud shadows. However, it is interesting that the retrieved AOD within the cloud fields is substantially higher (0.5 to 0.75) than the AOD in the cloud-free areas (0.20 to 0.35). On the other hand, the lower resolution cloud mask discards much more of the area, and the resulting retrieval has much fewer retrievals of high AOD.

Note that this flight line and most of the eMAS flight lines during SEAC^{4}RS are over land. Thus, the primary DT algorithm applied and presented in this study returns AOD, but not Ångström exponent or other indicators of particle size that is reported over ocean. Also note that unless stated, the analyses in this paper refer the ~0.5 km resolution (non-degraded) eMAS.

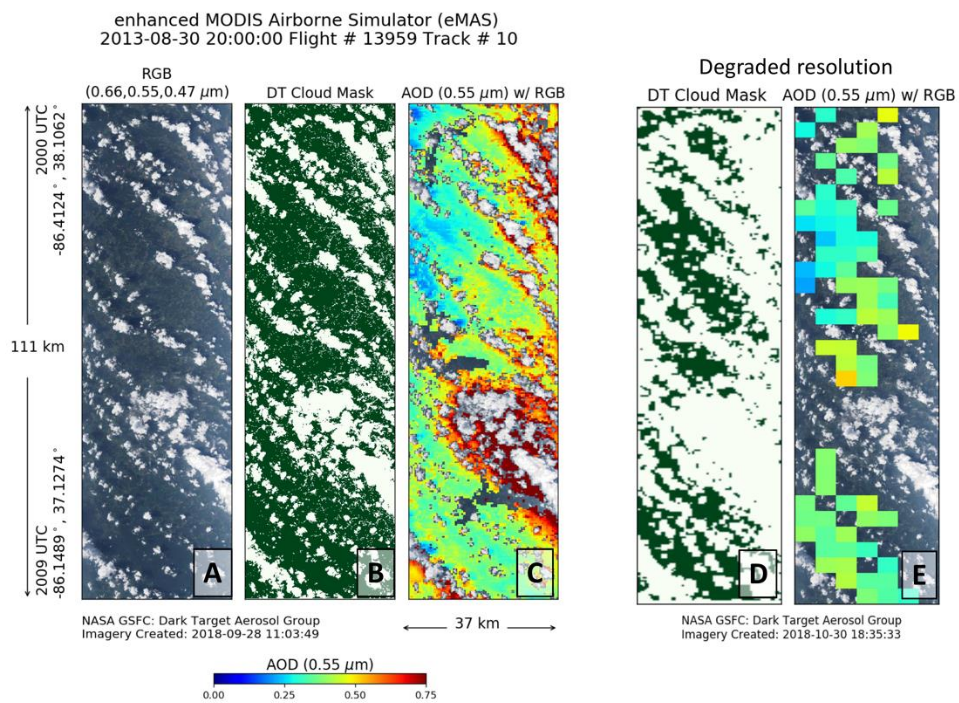

Figure 1: Sample imagery of the DT algorithm applied to SEAC4RS eMAS flight track 13_959, Track #10 on 30 August 2013 20:00UTC. Plotted from left to right are (A) true-color RGB at 50 m, (B) DT-aerosol cloud mask at 50 m, and (C) the retrieved AOD (at 0.55 μm) at 0.5 km. Panels (D) and (E) are DT-cloud mask at 500 m and retrieved AOD at 5 km, corresponding to degraded eMAS resolution.

3.3 AERONET

The Aerosol Robotic Network (AERONET, Holben et al. (1998)) provides ground-based measurements of spectral AOD using sun-observing radiometers. Measuring the extinction of direct sunlight in four or more channels (including 0.44, 0.67, 0.87 and 1.02 μm), spectral AOD is accurate to ±0.02 or better within clear skies (25% of the L2 data), sufficient as ground-truth for satellite AOD retrieval validation. AERONET has grown into a relatively dense global network of over 200 sites in continuous operation. The AERONET network was expanded during SEAC^{4}RS over the area of flight operations specifically to support the deployment, and flight plans revolved around the locations of AERONET sites. We have used Version 2 AERONET sun data to validate the DT eMAS aerosol retrievals during SEAC^{4}RS.

3.4 Cloud Physics Lidar

The Cloud Physics Lidar (CPL; McGill et al., 2002), a nadir-pointing elastic backscatter, was also deployed on the ER-2 during SEAC4RS. The CPL takes profiles of atmospheric backscattering, and was aligned to be co-located along the center (near-nadir view) of the eMAS swath (Meyer et al., 2016). The CPL operates at three wavelengths (355, 532, 1064 nm), enabling a comprehensive analysis of radiative and optical properties of aerosols and clouds. The high signal-to-noise ratio (SNR) of CPL measurements allows for accurate detection of optically thin cirrus clouds (COD < 0.3) (Sassen and Cho, 1992). Coincident CPL measurements provide vertically resolved aerosol properties that complement the passive aerosol products (i.e. AOD, aerosol type) and identify the vertical location of cloud and aerosol layers in complex scenes. These datasets correspond to ~200 m horizontal resolution (1 Hz sampling) and 30 m vertical resolution. Like previous studies that use lidars to evaluate cloud screening and aerosol retrievals from passive sensors (Su et al., 2008; Kittaka et al., 2011; Varnai and Marshak, 2012), we look to use CPL to evaluate our eMAS retrievals.

4 Analysis of eMAS aerosol data

4.1 Comparison of clear-sky AOD with MODIS

According to the eMAS website (SEAC4RS campaign), five flights were directly and simultaneously underneath either Terra or Aqua (MODIS) overpass. However, if tolerance of the temporal collocation with either MODIS is increased to ±30 minutes, there are 134 additional underpasses. Here we have settled on ±15 minutes which leads to 71 underpasses. An example from 19 August is presented as Fig 2, which is the AOD from eMAS matched with AOD from MODIS (Terra 3 km product), all superimposed upon the MODIS RGB image. Overall, there is remarkable agreement, and the AOD gradient matches well. One can also see there are spots where MODIS does not retrieve but eMAS does. This is a relatively bright surface, where presumably the MODIS-DT might throw out pixels at its native (0.5 km) resolution, but eMAS may find enough “dark” pixels at its native resolution (~50 m) to retrieve AOD.

Not all eMAS/MODIS AODs match as well as they do in Fig. 2. This case was unusual in that the ER-2’s flight direction matched Terra, and the flight path was reasonably close to the nadir view for MODIS. However, in many cases, the geometry of the eMAS observation is very different from MODIS, owing to different flight directions or that the eMAS flight is located close to the edge of the MODIS swath. At MODIS swath edge, individual pixels are up to 4x the size of those near nadir, and a few small clouds will make a MODIS retrieval impossible. Yet, eMAS, always viewing near nadir and at fine spatial resolution, might retrieve. Other poor matches occur when either instrument is observing close to the specular direction over water. Nonetheless, let us compare the aggregate of the 0.5 km eMAS retrievals encompassed within MODIS AOD retrieval boxes (both 10 km and 3 km).   The eMAS retrievals are defined by their center latitude/longitude.

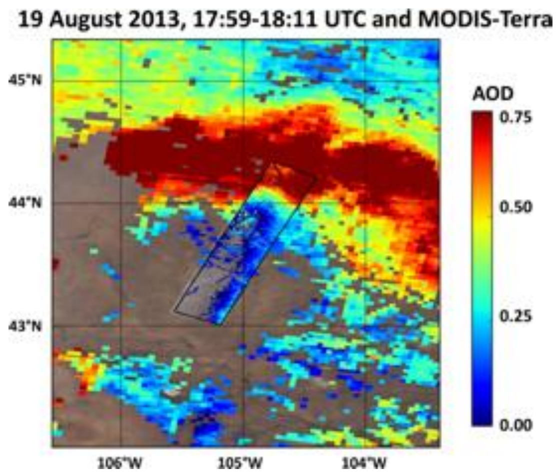

Figure 2: AOD (0.55 μm) from eMAS (Flight 13_955, Track #7, 17:59-18:11) superimposed on MODIS-Terra (3 km) observed at 17:40 UTC.

Fig. 3 presents scatterplots of eMAS AOD retrievals separately collocated with the 10 km and the 3 km MODIS aerosol products. Each solid dot represents the mean of 0.5 km eMAS pixels compared to the single MODIS pixel, whereas the error bars represent the standard deviation of the eMAS pixels. Each panel includes the 1-1 line (black line) and linear regression (red line + equation). Although there is slightly higher correlation when eMAS data are compared to 10 km than to 3 km data, the overall pattern is that where eMAS and MODIS both retrieve, eMAS is lower, except at very low AOD.

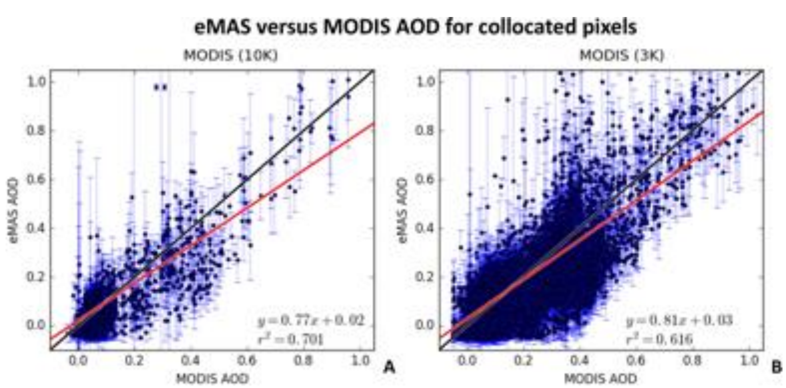

Figure 3: eMAS compared to MODIS AOD within ±30 minutes. (A) for 10 km MODIS data, and (B) for 3km MODIS data. Solid dots represent the mean of the eMAS AOD pixels compared to the value of encompassing MODIS AOD pixel; the error bars represent one standard deviation of the eMAS pixels. For each panel, the black line is the 1-1 line and the red line and equation represents the linear regression.

With a nadir/nadir match and eMAS oversampling, there may be more than 36 eMAS AOD retrievals within a MODIS 3 km box. Nominally, there are roughly 60. There also can be more, such as where a MODIS retrieval is stretched (up to 8x nadir size) near swath edges, thus encompassing more eMAS retrievals. However, when there are clouds or other non-retrievals, there will be fewer. Fig. 4 shows the Aqua-only 3 km scatter plot of Fig. 3 with the dots color-coded by the number (sample size) of eMAS retrievals within a MODIS one. As we see from Fig 4, eMAS tends to report higher AOD than MODIS for smaller sample size (i.e. sample size < 60) and lower for larger sample size (i.e. sample size > 90).

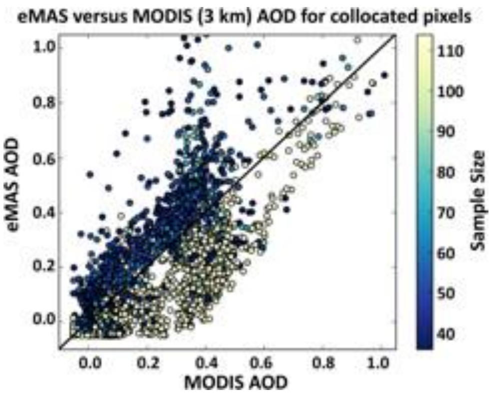

Figure 4:Spatiotemporal collocations of eMAS and MODIS pixels within 30 minutes of retrieval. eMAS pixels within a single MODIS (Aqua @ 3K) pixel are averaged and colored by their sample size. Sample size is proportional to the sample area resolution. In this case, sample size has a strong division, where small sample sizes of eMAS (cloudy) had a high bias and large sample sizes (clear sky) had a low bias, in comparison to MODIS. This separation exaggerates the low bias of eMAS and the potential effects of sub-pixel clouds

A possible explanation for varying eMAS-MODIS difference is varying cloud fraction. When sample size is larger (presumably less cloudy conditions), eMAS AOD tends to be relatively low compared to the MODIS retrieval. This could mean that when both sensors are under completely clear conditions, it may be calibration that leads to eMAS retrieval being “low”. However, another explanation is that spatial resolution still matters. While MODIS is performing its pixel filtering (cloud masking, and then throwing away 20% of the darkest and 50% of the brightest 0.5 km pixels), it is still missing subpixel clouds. When eMAS is doing its own filtering at higher resolution, these clouds are successfully removed. In other words, instead of interpreting eMAS as being biased low, MODIS may be retrieving high due to subpixel clouds.

On the other hand, when the eMAS sample size is smaller, there are presumably more clouds. By performing its native pixel filtering, the standard MODIS over-land retrieval is supposed to be eliminating not only clouds (the cloud mask), but preferentially eliminating cloud edges and adjacency effects. Yet at a cloud edge, it is possible that eMAS may report 0.5 km AOD (even with its own 20% and 50% filtering of 50 m pixels). This will mean that in more cloudy conditions, eMAS would be retrieving some of the near-cloud aerosol information, and thus show higher AOD compared to MODIS.

Levy et al. (2013) report retrievability (or availability) of MODIS-DT to be approximately 10% on a global scale, meaning that there is close to 90% failure due to clouds, glint, bright land surfaces (deserts, ice/snow, urban) or other reasons. The success rate improves somewhat if desert or ice/snow targets are excluded from the denominator, but overall retrievability remains well below 20%. Recall in Fig. 2 that eMAS and MODIS compare well when reporting the overall AOD gradient. However, we also see that eMAS is retrieving in areas that MODIS does not. Presumably the finer resolution eMAS is providing sufficient opportunity to find holes between the clouds (or green spots within bright targets).

Fig. 5 reports on the successes and failures of collocated MODIS and eMAS pixels. Based on all 71 cases where eMAS and MODIS report within ±15 minutes, there are four categories: both retrieve, neither retrieves, only eMAS retrieves or only MODIS. The left panel illustrates the 2x2 matrix, plus some reasons for each case. Other than the scene changing (clouds appearing within ±15 minutes), there are very few reasons why eMAS should fail (while MODIS succeeds). Of course, eMAS could have poor conditions for observation, for example observing in glint while MODIS does not. This also can happen vice-versa. But, based on resolution only (e.g. Figure 1), it is more likely that eMAS succeeds where MODIS fails.

The right panel of Fig. 5 shows frequencies of each category. In ~10% of the time, both eMAS and MODIS retrieve AOD. In ~60%, neither retrieves. There are cases where MODIS retrieves but not eMAS, but this is <2% of the time. There are many more, ~20%, where eMAS retrieves but not MODIS. In summary, MODIS behaves as it always does, in that it retrieves in <20% of the cases and fails in >80% of them. However, there are a significant number of extra retrievals from eMAS that can provide previously untapped information about aerosols in situations impossible for MODIS to observe.

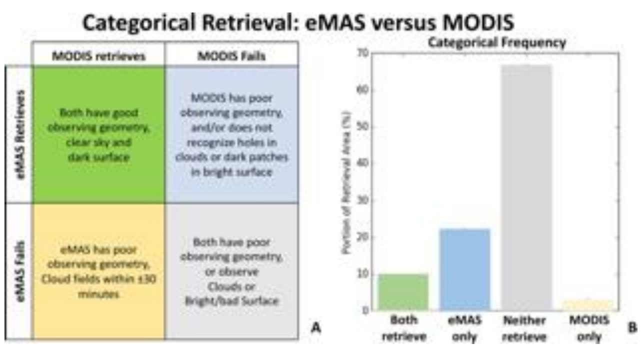

Figure 5:Categorical description to represent different combinations of eMAS vs MODIS retrieval success, along with (A) some possible reasons and (B) Frequency for each category, based on the MODIS 10 km product.

Fig. 3 showed that where there are both eMAS and MODIS retrievals, eMAS AOD tended to be offset low, especially in cloud-free cases (Fig. 4). In the 20% of cases where eMAS retrieves but MODIS fails, what is the character of the eMAS-retrieved AOD? Fig. 6 presents AOD histograms, comparing the distribution of eMAS retrievals where MODIS retrieves and where MODIS fails. While there are small differences between 3 km MODIS and 10 km MODIS histograms, both show large differences between when MODIS also retrieves (green) and where MODIS does not (blue). In this sample, there is an average enhancement of 0.35 (nearly 350%) for the mean value of AOD when MODIS has failed. In other words, *based on what eMAS observes, MODIS is missing retrievals containing an additional 0.35 of AOD*.

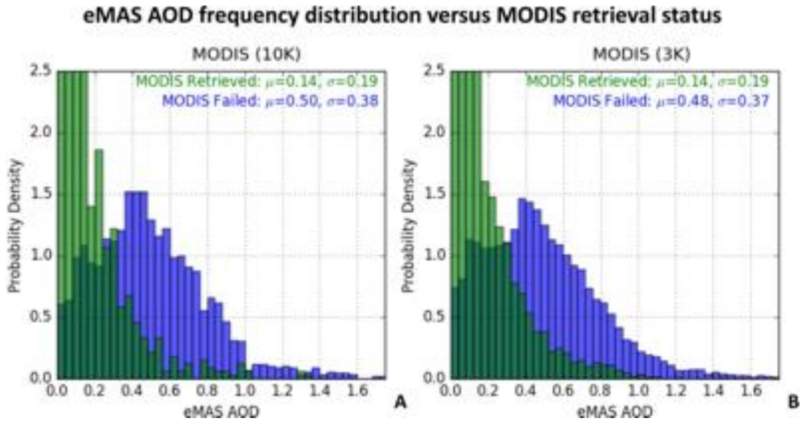

Figure 6: The eMAS AOD frequency distribution when there is success (green) or failure (blue) by MODIS ((A) = 10 km, (B) = 3 km)). Overall, there is a mean AOD enhancement of more than 0.34 (~220%) when eMAS retrieves within MODIS failed areas.

What is this additional AOD? We might explain it as more particles produced from cloud processing, enhanced AOD from the same number of particles swelling with humidity into a more optically efficient size, cloud contamination, or an adjacency effect. In the next subsections we compare the eMAS retrievals with other datasets, and show that much of the enhancement is likely to be cloud adjacency (3-D radiation) effect.

4.2 Comparison of clear-sky AOD with AERONET

The spatio-temporal statistical method (Ichoku et al., 2002; Petrenko et al., 2012) is used to collocate satellite-derived or high altitude AOD retrievals with AERONET ground based observations. This compares the spatial average of the retrievals (centered at the AERONET site) with the temporal average of ground observations (centered at time of overpass). The size of the spatial domain impacts the correlation between the satellite and ground-based observations. When comparing the MODIS 10 km product with AERONET, the spatial domain is generally accepted to be within ~±25 km (radius or half of square edge) of the AERONET site. However, when comparing higher-resolution data (e.g. the 3km product), Munchak et al. (2013) and Remer et al. (2013) show that ~±7.5 km radius was more appropriate.

Here, we determined the spatial averaging criteria for eMAS versus AERONET by trial and error. All possible valid matches (AERONET within ±30 minutes and eMAS within a radius of 25 km) were collected. The search radius was gradually increased (starting with 1 km). This resulted in rapidly increasing the number of valid collocations, as well as increasing the correlation (r-squared). The sample size and correlation plateaued at ~6 km radius, suggesting a fair balance between representing spatio-temporal statistics while still representing fine resolution structure in the retrieval. The +/-30 min provided a small enough window to avoid significant changes in atmospheric conditions while also obtaining two or more AERONET measurements (to average) as their typical time series interval is set at 15 minutes. Note that when performing the collocation, AERONET AOD data were interpolated to 0.55 µm (to match the eMAS retrieval), by using the 2nd order regression curve of a log-log plot (Eck et al., 1999).

Using the 6 km radius and ±30 minute interval, there were 57 collocations of eMAS tracks over ground-based AERONET sun photometer sites. These 57 collocations occurred within 43 eMAS flight tracks, as some tracks included more than one AERONET site. Fig. 7 presents a map of some of these collocations over the eastern U.S., showing repeated flights (and 22 of the collocations) over AERONET sites near Houston, TX (https://aeronet.gsfc.nasa.gov/new_web/DRAGON-USA_2013_Houston.html). The mean of the AERONET AOD is represented as the filled inside of a ring, whereas the mean of the eMAS retrieval (within 6 km) is the outer ring.

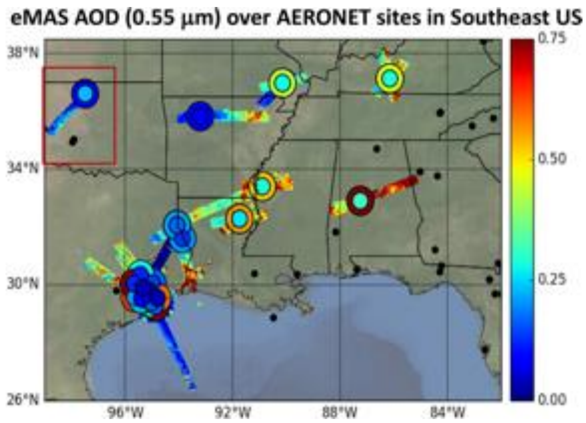

Figure 7: eMAS tracks and AERONET measurements collocated within a 6 km radius and a time window of +/- 30 min. The AERONET measurements are represented by the inner circles while the eMAS collocations are represented by the outer rings. This map shows only the collocations over the southeastern united states, but collocations that occurred in California were also accounted for in the analysis. The red box relates to the collocation described as Fig 9F.

Fig. 8 compares AOD (at 0.55 µm) for all 57 eMAS/AERONET collocations within 6 km and ±30 minutes. Generally, eMAS AOD is higher than AERONET. If we sort the collocations by the number of eMAS 0.5 km retrievals within the 6 km radius, we isolate 67% (38 red-ringed points) with the larger sample sizes (more eMAS pixels within a given collocation). The regression in Fig 8 is created from the ringed dots only, showing that eMAS-retrieved AOD is high (slope = 1.85) compared to AERONET. Presumably representing cloudier scenes, the collocations made with fewer eMAS pixels tend to show even larger offset. This is not surprising considering the histograms shown in Fig. 6, but curious considering the overall low AOD compared to MODIS in mutually cloud-free scenes conditions (Fig. 3). However, we also note that Houston is an urban area, and so a consistently high AOD compared to AERONET could also be representing the known C6 retrieval bias in urban areas (e.g., Munchak et al., 2013; Gupta et al., 2016).

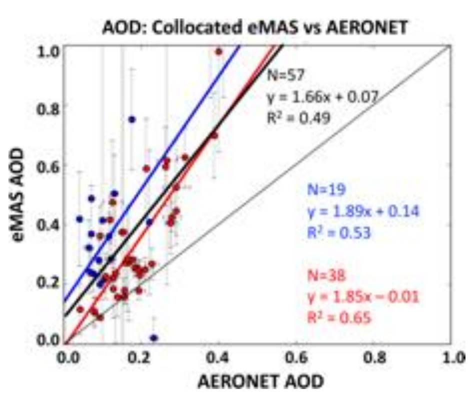

Figure 8: Scatter plot of collocated eMAS and AERONET AOD. Each point represents a spatial mean of eMAS retrievals within a 6 km radius of the AERONET station and a temporal mean of AERONET observations within +/- 30 minutes of eMAS

overflight. The y-error bars are the standard deviation of the eMAS AOD pixels. The three regression lines are fit to all 57 points (black), to the 38 points which have larger eMAS sample size (red), and the 19 points with smaller sample size (blue).

Looking closer at Fig. 7, while the eMAS-retrieved AOD closest to the AERONET site (outer ring) is higher than AERONET-observed AOD (inner ring), somewhere within the flight track there is closer agreement. Fig. 9 details five of these flight tracks, showing that while the mean of the eMAS-retrieved AOD within 6 km of the site is larger than that observed by AERONET, there are also retrievals within 10 or 15 km of the AERONET site that match more closely. Interestingly, there is a case shown in Fig 9 (location shown in Fig 7), which was the only three-way collocation (eMAS/MODIS/AERONET) during SEAC^{4}RS. This extremely clear scene shows the opposite behavior, as the close-in eMAS AOD tends to be lower than AERONET.

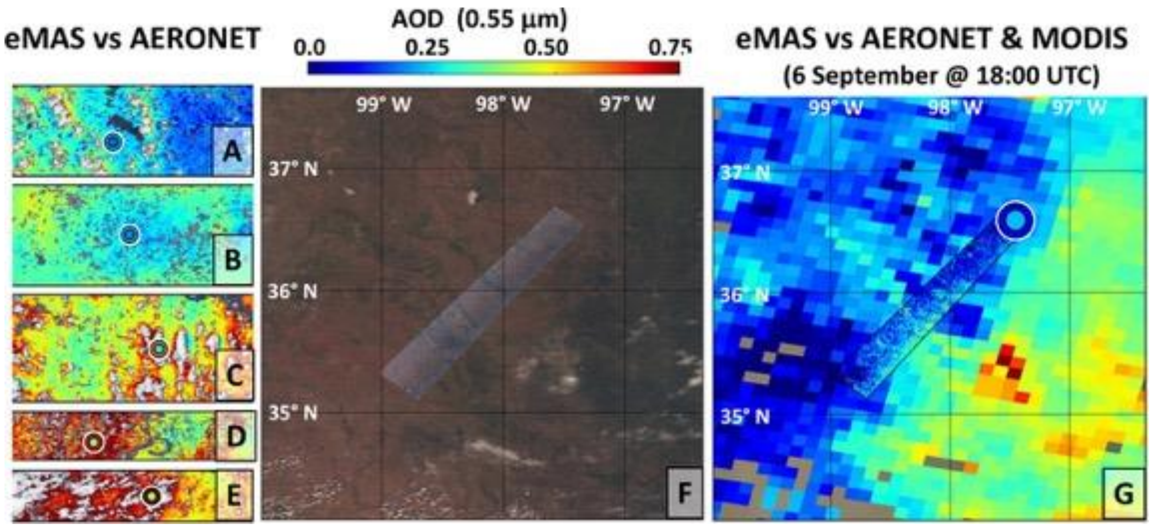

Figure 9: Left, Panels (A)-(E): eMAS/AERONET AOD collocation (rings) superimposed on eMAS AOD. Inner rings are averaged AERONET AOD (±30 minutes) while outer ring is averaged eMAS AOD (6 km radius). eMAS Timestamps (track numbers) over AERONET site (lat, long) from left to right: (A): 9 September 20:37 UTC (Flight 13963 Track #11) over Carthage site (32.06, -94.07); (B): 9 September, 22:19 UTC (Flight 13963 Track #16) over Baskin (32.28, -91.74); (C): 30 August, 19:17 UTC (Flight 13959 Track #07) over IMPROVE-MammothCave (37.13, -86.15); (D): 9 September, 20:52 UTC (Flight 13963 Track #12) over Leland_HS (33.40, -90.89); (E): 30 August, 17:59 UTC (Flight 13959 Track #03) over SEARCH_Centerville (32.90, -87.25). Right, (F) and (G): RGB (true-color) and AOD from the three-way collocation between eMAS/AERONET and MODIS 10 km retrieval, where the ring represents eMAS/AERONET collocation.

In addition to urban surfaces (Houston), there are likely cloud effects that contribute to enhanced AOD. Clouds can introduce significant scattering of sunlight into the adjacent scenes, causing these areas to appear brighter to imagers above, resulting in higher values of retrieved AOD. Conversely, the AERONET instruments measure the direct transmittance of photons through the atmosphere, mostly avoiding any of the cloud-scattered photons, and are effectively immune to enhancements from adjacency effects. In fact, if sunlight were to be scattered by clouds into the AERONET instrument's field of view, the result would be an enhancement of transmittance (from forward scattering) that would be interpreted as a decrease, not increase, of AOD. Thus, while AERONET should observe enhanced AOD from new particle generation or swelling from humidity, AERONET would observe decreased AOD due to adjacency effects (assuming it passes through the cloud screening). We will look at this phenomenon in more detail within Section 5.

4.3 cloud masking

The DT aerosol cloud mask is a series of tests. Based on a visible-wavelength band (0.47 µm or 0.55 µm depending on land or ocean) and a cirrus-detection band (1.88 µm for MAS), a native-resolution pixel is considered a cloud if the absolute reflectance exceeds a threshold or the variability in the 3x3 box surrounding that pixel exceeds a threshold. In addition, results of four IR-based tests are read in from the MxD35-like product. As the DT algorithm was being developed, the combination of tests proved to be most protective of the DT product; effective at removing cloudy pixels, while leaving pixels suitable for aerosol retrieval.

The full MxD35-like cloud mask, however, includes an additional ~30 tests to determine the likelihood of a cloud in a given pixel, the results being “clear”, “probably clear”, “probably cloudy” or “cloudy”. Fig. 10 illustrates the difference between the DT aerosol cloud mask (middle panels) and the MxD35-like cloud mask (top panels) for two cases, where the MxD35 cloudy is the union of “probably cloudy” and “cloudy”. The bottom panels show the differences (aerosol-MxD35) for each case. In the difference panel, black pixels represent where the aerosol cloud mask (primarily based on spatial variability) identifies a cloud whereas the MxD35 version does not.

The first case (left panels) is from 30 August at 20:00 UTC, which is from flight 13_959 Track #1 (Fig. 1) crossing southward over southwestern Kentucky. Here, the aerosol cloud mask identifies more clouds, ensuring that a clear sky pixel is truly clear. This conservative bias results in wider cloud boundaries and less noise in the cloud-free sky. The second case (right) is from 6 September at 20:25 UTC, which is a scene from flight 13_962 and track #13 that traveled northeastward through northern Missouri. In this scene, the aerosol cloud mask clearly considers surface artifacts (farms, fields and roads that have highly variable reflectance) to be clouds. The masking of these artifacts at high-resolution is a further conservative measure to keep inappropriate pixels, including inappropriate surface types, from being used in the aerosol retrieval.

Considering flight tracks from the union of 30 August and 6 September, the cloud masks agreed (either both clear or both cloudy) for 83.0% of all pixels. The DT algorithm identified an additional 16.7% of pixels as cloudy that were not identified as cloudy by the standard cloud mask. Only 0.3% was masked by the standard mask without being flagged by DT. This example shows that the DT aerosol cloud mask may even be over-zealous at protecting the aerosol retrieval. In other words, the high AOD bias, when compared to AERONET is not explained by low-cloud contamination (unmasked low cloud) in the eMAS retrieval. It may also be possible that both the cloud-products and DT cloud mask may be missing optically-thin cirrus cloud (e.g. Holz et al., 2016; Marquis et al., 2017). We will discuss high-thin cirrus later in this section.

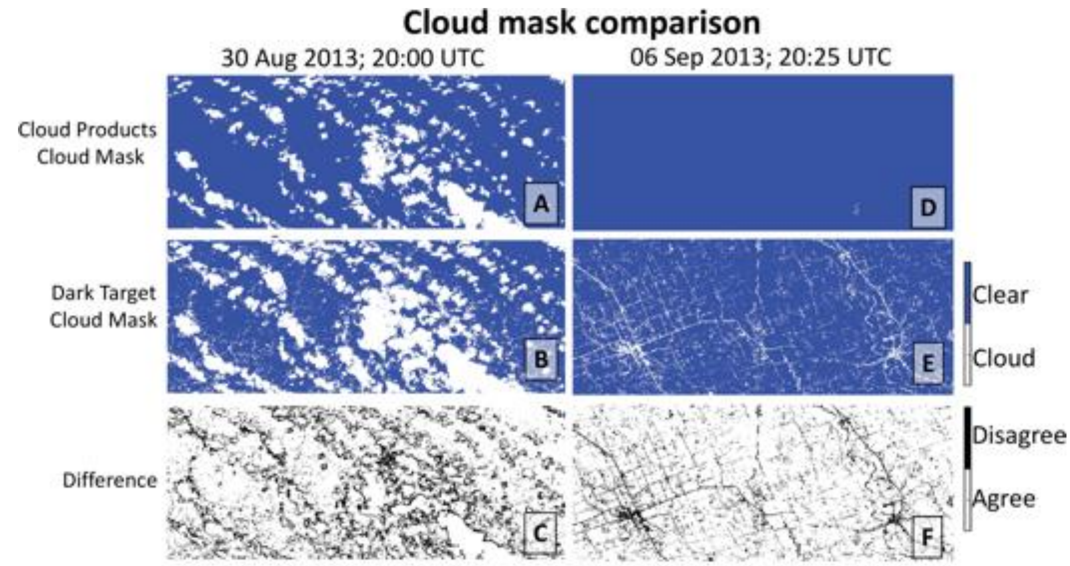

Figure 10: Comparison between DT and MxD35-like cloud masks for 30 August (A,B and C) and 6 September (D, E and F). Top, and middle panels are results from the MxD35-like and DT masks, respectively, where white color represents pixels identified as "cloud". The bottom panels are the difference, where black shows difference (DT – MxD35-like). Almost every black pixel is the DT algorithm identifying more non-retrievable pixels than the MxD35 cloud mask.

Unlike an imager that may observe light being reflected off of adjacent objects (e.g. clouds) that are not within the targeted pixels, a lidar observes only the return of emitted light pulses that are backscattered from specific targets. Side scattering into the lidar's field of view from adjacent objects provide negligible enhancement as compared with the active return from the target. Therefore, a lidar can help to validate imager cloud masks, as demonstrated by the many studies that have used lidar data from CALIPSO to validate cloud identification schemes from different imagers (e.g. Hutchison et al., 2014; Kopp et al., 2014; T. Wang et al., 2016; Kim et al., 2017; Marquis et al., 2017).

During SEAC^{4}RS, the Cloud Physics Lidar (CPL) flew on the ER-2 with eMAS, deriving a range of atmospheric and surface products from the measured backscatter returns. These data products include 'Layer Type', which identifies clouds, layer by layer, throughout the entire atmospheric column. The CPL is particularly sensitive to thin clouds (e.g. Davis et al., 2010), which may be missed by both the DT aerosol cloud mask and the standard MxD35 cloud mask applied to eMAS data. CPL is measuring very close to the nadir view along the center of the eMAS flight swath, with products provided at ~200 m horizontal resolution. This means that at ~40-50 m (native) resolution, there are ~20 eMAS pixels within each CPL pixel.

For the union of the flight tracks analyzed from 30 August, there are approximately 14,000 CPL columns along track. We can compare the clear/cloud detections from the CPL with the nadir results from both eMAS cloud masks (DT and MxD35-like). While CPL cloud fraction is binary (clear=0 or cloudy=1), the eMAS cloud fraction can be between 0 and 1.

Consistent with Marquis et al. (2017), we see that the MxD35-like cloud mask is in strong agreement with the CPL for clear skies. On the other hand, when CPL detects a cloud, the MxD35-like cloud mask misses about 25%, with 17% denoted to be entirely clear of clouds. This disagreement may suggest the presence of high cirrus that goes undetected, or it may reflect this mask's purpose in identifying pixels appropriate for a cloud retrieval.

In terms of the DT aerosol retrieval, when CPL identifies a cloud, DT finds some fraction of cloud within the grid box 95% of the time. However, DT misses a CPL cloud nearly 5% of the time, which we cannot easily explain. However, even if the DT aerosol cloud mask misses 5% of clouds, the effect on the final retrieval will be negligible, as the algorithm further purges another 50% of the brightest pixels within the grid box after cloud masking and before making a retrieval. Presumably, residual cloudy pixels will be eliminated in this purge. While the DT cloud mask leans towards agreement with CPL for cloud-free skies, over 60% of CPL cloud-free pixels are associated with DT aerosol 10x10 boxes reporting at least some fraction of cloud. Likely the cloud in these 10x10 boxes is not actually coincident with the 200 m CPL footprint. DT is aggressive in its cloud masking in order to protect the aerosol retrieval from marginal conditions. Overall, the DT aerosol cloud mask appears to be protecting the aerosol retrieval from cloud contamination.

4.4 Cloud Organization

In the above analysis of eMAS AOD, there is enhanced AOD due to proximity to clouds. It does not appear that it is due to simple cloud contamination (undetected or unmasked cloud). Therefore, this high AOD retrieval may be due to either changed aerosol properties (e.g. swelling in humidity near clouds, new particle generation or cloud processing of particles), or an adjacency effect (e.g. radiation being reflected from nearby clouds). We can compute three parameters that define the relationship of a cloud-free pixel to its cloudy environment: (1) the distance to the nearest cloud, (2) the direction of the cloud with relation to the sun, and (3) the cloudiness of the immediate environment or the cloud density. Each of these three parameters may have a different effect on the remote sensing of aerosols (see Varnai et al., 2017).

Similar to the C6 MODIS products, our DT aerosol product on eMAS includes a native resolution cloud mask (i.e., 50 m). However, as shown in Fig. 10, the DT cloud mask is also identifying surface features and other inhomogeneous features as “cloud”. The overzealous cloud mask is protecting the aerosol retrieval from inappropriate retrieval scenes, but makes it difficult to analyze cloud-only effects on the retrieval. Therefore, we derived alternative cloud distance values from the less aggressive MxD35-like cloud mask, which we believe better identifies true clouds in our example scenes. Let us define “distance to the nearest cloud” and “cloud fraction”, based on the derivations from the MxD35-like cloud mask. The “distance to cloud” will refer to the average distance to the nearest cloud of all cloud-free 50 m pixels within the 0.5 km retrieval grid box corresponding to one AOD retrieval.

Although cloud masks will discard both clouds and cloud shadows, in otherwise clear pixels, there will be radiation scattered from the sunward side and shading from the shadowed side. These are adjacency effects. For each cloud-free 50 m pixel, the direction to the nearest cloudy pixel was determined and then mapped to a coordinate system defined by the relative positions of the averaged sensor and solar azimuth angles. This resulted in an angle of 0 degrees for a retrieval that occurs on the sunward facing side of the cloud, and an angle of 180 degrees when on the shadow side of the cloud (Fig 11E). To simplify, we denote ±(0°-45°) as "Sunny Side", ±(45°-135°) as "Neutral Sides", and ±(135°-180°) as "Shadow Side".

We demonstrate these parameters in the case study of 9 September 2013 at 18:41-19:09 UTC (Flight 13363, Track #6). This track flew southward over the Texas/Louisiana border and into nearby coastal waters, and overflew two AERONET sites (Calipso_Carthage (-94.066°, 32.064°), Calipso_Sabine_Frst (-93.867°, 31.607). Figure 11 plots RGB, DT cloud mask, retrieved AOD, distance from cloud, and solar direction for this flight track. It also plots the associated eMASL2CLD (MxD06-like) retrievals of cloud top temperature, cloud phase, and ice cloud optical thickness. The solar zenith angle (SZA) is 27.45°. The AOD (panel G) is overplotted on the RGB, and also displays the locations of the AERONET sites, and the CPL cloud detections (black stripes) over the nadir (center) track.

For this case, retrieved AOD is smallest where the cloud field is least dense (colder colors in Cld_Dist panel H). The AOD values appear to match closely with the observations at the AERONET sites. There is no obvious visual relationship of AOD with the solar direction and there is minimal appearance of cloud shadowing with this SZA. We also highlight a small portion (outlined in white lines) where ice clouds were detected by 1.88 μm thresholds (>0.025) and retrieved by the eMAS cloud retrieval. These ice clouds appear to have cloud optical depth on the order of 0.3, suggesting that even thinner ice clouds could have escaped detection by the DT cloud mask (e.g. Holz et al., 2016; Marquis et al., 2017). However, using simple phase function analysis (e.g. Pierce et al., 2010), it is not likely that the corresponding reflectance in the visible channels would lead to such a significant AOD enhancement. Unfortunately, at this time, noise in the eMAS 1.88 μm channel precludes lowering thresholds to detect more high clouds.

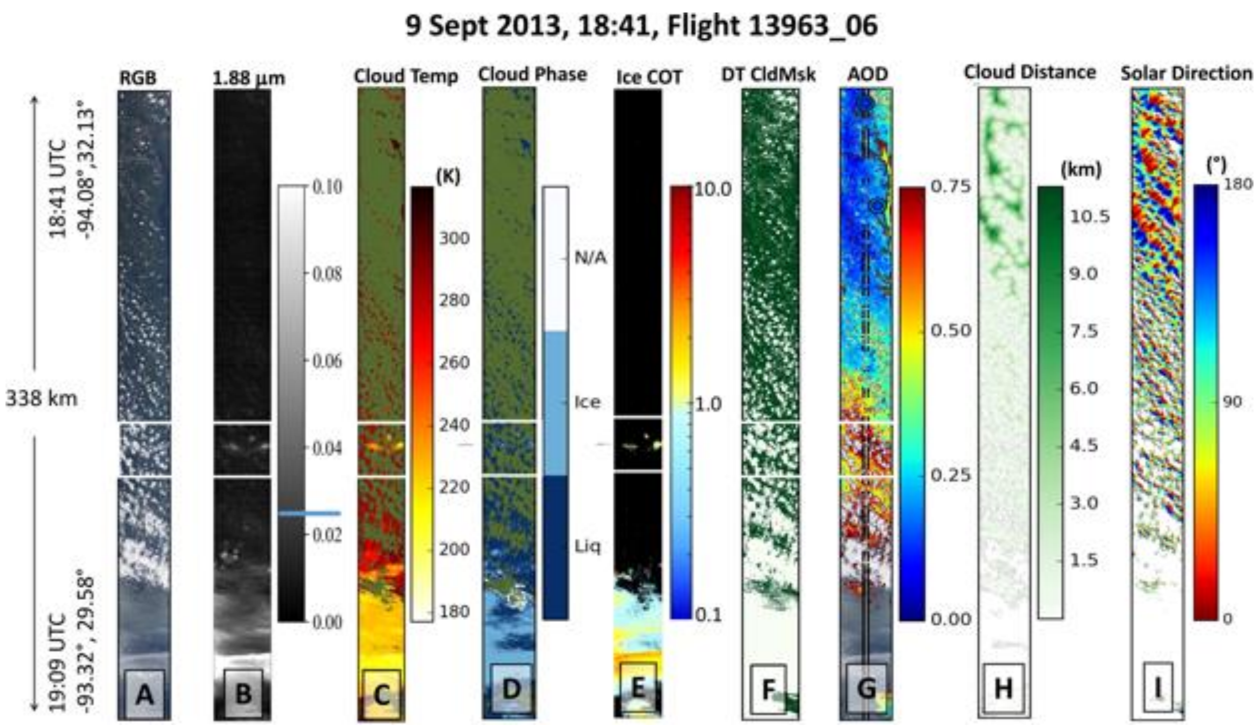

Figure 11: eMAS aerosol and cloud retrievals from 9 September, 18:41 UTC (Flight 13963, Track #06), including (A) RGB and (B)1.88 μm reflectance, (C) Cloud Top Temperature, (D) Cloud phase, and (E) Ice cloud optical thickness, (F) the DT cloud mask and (G) retrieved AOD. Also plotted are calculations of the nearest cloud pixel in (H) and solar direction (I) of the nearest cloud using the cloud-products cloud mask (not shown). The AOD layer in (G) is superimposed onto the RGB image and includes AERONET (Calipso_Sabine_Frst and Calipso_Carthage sites) and CPL data. The AERONET measurements are represented by the inner circles while the eMAS collocations are represented by the outer circles. The CPL detection of clouds is represented by the two parallel lines that run down the centerline of (G). The white parallel lines (Panels (A) – (G)) outline a small area characterized by thin ice cloud detection (above 1.88 μm threshold – blue line in (B) color bar) and retrieval.

Fig. 12 presents some statistics for the imagery plotted in Fig. 11. Fig. 12A is a 2-D frequency histogram, comparing retrieved AOD with the average distance to the nearest cloud within the AOD retrieval grid box, and also with the AERONET data from the two sites (averaging 0.13). Clearly, retrieved AOD is greater close to cloud. Applying the normal collocation method (averaging all eMAS data within 6 km of the AERONET sites) yields eMAS AOD value of 0.19 (a high bias of 39%). Weighting this collocation toward pixels far-from-cloud (e.g. > 6 km) yields AOD of 0.125 (3.9% lower than AERONET), while weighting toward pixels close-to-cloud yields AOD value of 0.24 (nearly double). Note that nearly 75% of all retrievals in this track are within 2 km of clouds.

Fig 12B shows the mean AOD and standard deviations, separated into the three different cloud illumination geometries, as a function of distance-to-nearest cloud. When closer than 2 km, the shadow side is lower by 0.08 AOD, as compared with the sunny and neutral sides. We stress that in this case, the SZA angle is shallow enough so that cloud illumination/shadowing effects are small. There are other eMAS cases with deeper clouds and/or steeper SZA, where we expect the differences in geometry to gain greater prominence. Fig. 12B suggests that a part of this near-cloud enhancement is due to geometrically dependent adjacency effects, but only within the nearest 2 km of the cloud, whereas the observation of high bias begins within 5 km of cloud.

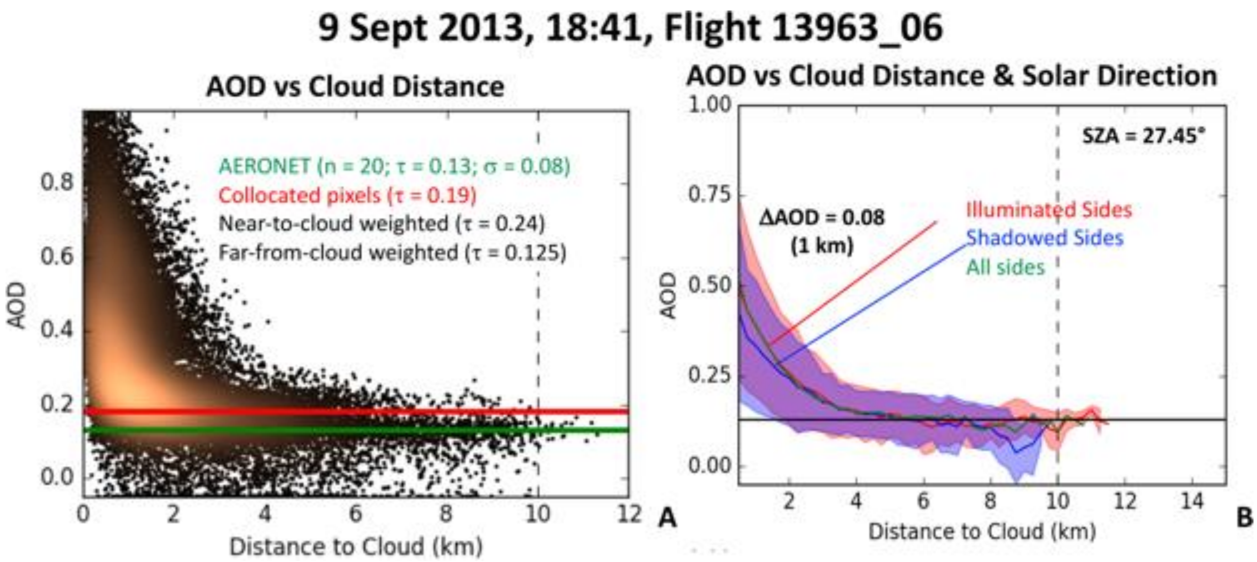

Figure 12: Using the example flight track, retrieved eMAS AOD is compared to the distance to cloud. (A) Density histogram of all points within the image. Superimposed on this histogram are lines corresponding to the averaged AERONET (AOD=0.13±0.08, in green) and averaged eMAS (AOD=0.19, in red) collocated within 6 km of the two AERONET sites. Weighting the collocations to retrievals close-to-cloud yields AOD=0.24, whereas weighting to retrievals far-from-cloud yields AOD=0.13. (B) Similar to panel (A), but also separated by solar direction with respect to the sun (zenith angle of 27.45°) and the clouds (red-illuminated side; blue-shadow side). The lines are mean for each side, whereas shadings represent standard deviation. At 1 km from cloud, there is 0.08 difference between illuminated and shadowed cloud sides

.

For flight 13963 track #06 (Figs. 11-12), we found that eMAS AOD strongly increased as the retrieval approached clouds. Obtaining “background” AOD (AERONET value of ~0.13) required the retrieval to be at least 5 km from clouds. Would the overall high bias of eMAS retrievals against AERONET observations in SEAC[4]RS be reduced if we weighted each retrieval within the spatial collocation radius by the inverse of its average distance to the nearest cloud?

Fig. 13 is the validation of the eMAS AOD in which the value of each collocation is inversely weighted toward retrievals far-from-cloud (e.g. “background” AOD). When compared with Fig. 8, the standard deviation of the eMAS is reduced, the regression slope reduces from

1.85 to 1.29 and yet the correlation (r-squared) remains the same. Note that N=43 (instead of N=57 in Fig. 8) because we are assuming there is a background AOD for each of the 43 eMAS/AERONET collocated flight tracks. This plot further supports the hypothesis that near-cloud effects are likely introducing a high bias in the retrievals.

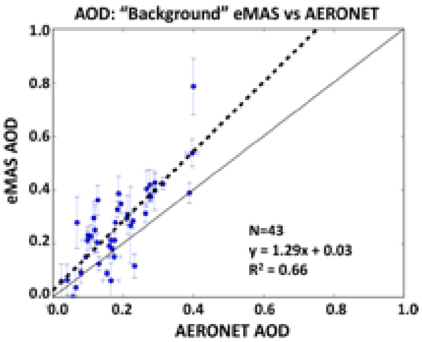

Figure 13: Scatter plot of collocated eMAS and AERONET AOD, where the eMAS AOD is weighted toward its "background" level far from clouds and the AERONET value is temporal mean +/- 30 minutes of eMAS overflight.

4.4 Cloud Density

Noting the large scatter of points in the AOD vs. distance to cloud in Fig. 12A, it is clear that distance to cloud alone does not explain the variance. Most of this variance occurs where the average distance to the closest cloud pixel is small. Using either the DT or the standard MODIS cloud masks, one can derive a cloud fraction for each 0.5 km retrieval. However, a problem with a simple cloud fraction is that there is no knowledge of the clouds outside of this retrieval box. A clear scene can be surrounded by clouds, or vice versa, so the local cloud fraction may not sufficiently characterize the overall cloudiness of the nearby environment. Here, we use the MxD35-like cloud mask and cloud distance field to derive a weighted cloud fraction, which we term the "cloud density". We choose to use a weighted cloud fraction rather than a simple cloud fraction in a larger box to tie each retrieval to the local cloudiness more tightly, but still acknowledge the effects of cloudiness in the overall cloud field (Bar-Or et al., 2010).

As illustrated in Fig. 14, each 0.5 km retrieval box is assigned the weighted average of all cloud fractions of all retrieval boxes within 10 km. This creates a 20 km x 20 km bounding region, with weights given by

$$W_j = \exp\left(-\frac{x-1}{b}\right) \quad , \qquad (1)$$

where W_j is the weight of a retrieval box in the sample, b is the characteristic decay parameter (in numbers of retrieval boxes), and x is the distance (in numbers of retrieval boxes) from the center value. This results in a weight of 1 when the sample retrieval box is directly adjacent to the center box and a weight of 0 when it is infinitely far from it. The density for the center value retrieval box then becomes

$$\rho_i = \frac{\sum_{j=1}^{n} W_j CF_j}{\sum_{j=1}^{n} W_j} \quad , \qquad (2)$$

where ρ_i is the center value retrieval box density, CFj is the cloud fraction of an adjacent retrieval box, and Wj is the weight of an adjacent retrieval box. The center value box, ρ, becomes a dimensionless value between 0 and 1, where 0 represents clear sky conditions and 1 is fully cloudy conditions. This process is then repeated for all i boxes in the scene. Through iterations, the b parameter will be chosen to maximize correlation. Retrieval boxes within 10 km of the swath edge will be affected by incomplete boundary regions, and so the cloud density is only retained for retrieval boxes lying within the center 15 km of the 35 km-wide swath.

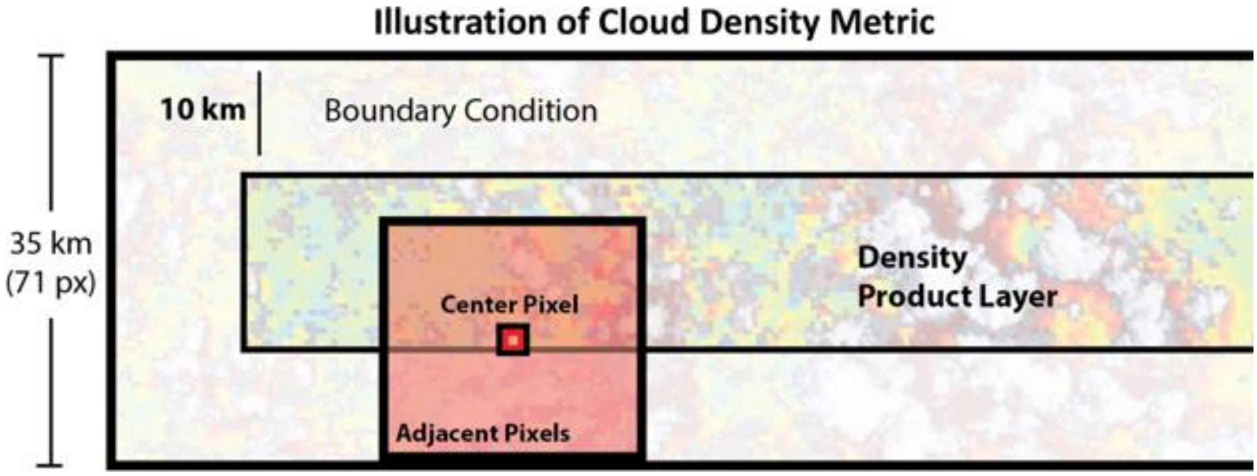

Figure 14: An illustration for the density layer algorithm. Each eMAS retrieval (labeled as center pixel) takes on the weighted average of the MxD35-like cloud fractions for all retrieval boxes (labeled adjacent pixels) within 10 km from it. The red bounding box serves as the kernel that scans the entire cloud mask for clouds in the adjacent pixels and returns a cloud density value (between 0 and 1) in the active center pixel. Due to the boundary condition and the width of the kernel, the final density product is trimmed by 10km.

For the same flight track of Fig. 11, Fig. 15A shows the AOD as a function of cloud density based on a fitted decay curve, with b from Eq. 1 equal to 8. This density decay curve has an e-folding distance of 4.5 km (9 retrieval boxes at 0.5 km resolution) and results in correlation between AOD and the 2-dimensional cloud density of r^2=0.80, which greatly improves on the r^2=0.32 explained by cloud distance only. Using the calculated regression equation, the AOD is regenerated as "Modeled AOD" (Fig. 15B) to visually illustrate the correlation with the measured AOD. This strong correlation may be improved even further by combining this one parameter regression with the shadow effects observed within 2 km of cloud, or by fitting a non-linear function to the points in Fig. 15A. Note that as this cloud density is based on MxD35-like cloud identification, there are fewer gaps in the modeled AOD field (Fig 15B) versus the retrieved AOD (Fig 15C) which is based on DT-aerosol cloud mask. In this case, the linear regression line provides a model for AOD enhancement. The y-intercept of 0.10 represents the mean clear sky AOD, which agrees closely with the distance to cloud method in Fig. 12. The slope then provides theoretical enhancement that would be observed if an AOD retrieval were increasingly surrounded by clouds.

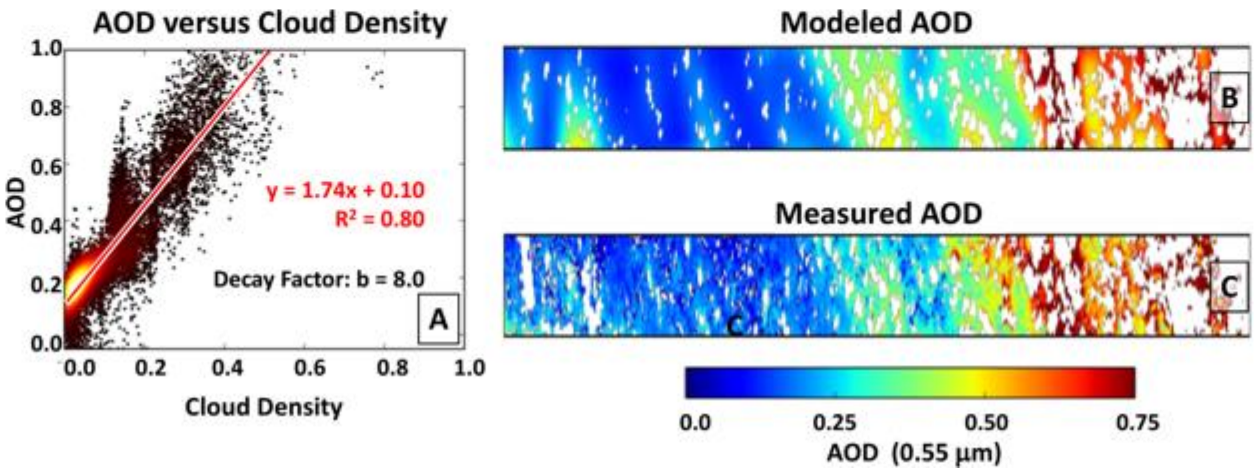

Figure 15:For 9 September, 18:41 UTC (Flight 13963, Track #06) eMAS AOD versus Cloud Density as derived from the MxD35-like cloud mask.(A): The scatter plot of all pixel values in the scene show the resulting relationship between cloud density and AOD using decay factor of b=8.0. (B): Modeled AOD image derived from the linear regression fitting presented in (A). (C): eMAS retrieved AOD at 0.55 μm.

Though this method had exhibited a strong correlation for this particular case, correlation is not as strong for others. There are many factors that change between scenes that prevent cloud density from being a dominant explanation of AOD variance. For instance, it does not account for cloud type or cloud height (Marshak et al., 2008), the surface (Wen et al., 2016), the aerosol itself, or overall meteorological conditions, all which would have varying effects on AOD enhancement. Other metrics besides cloud distance, cloud fraction and cloud density have been used to characterize different aspects of the cloud-aerosol relationship at other scales of interest (e.g. Bar-Or et al., 2010). The cloud density analysis, here, gives us a new method to quantify the link between AOD and clouds, and to create a statistical model to describe that link. However, the analysis cannot determine the physical reason for the enhanced AOD in situations with higher cloud density.

4.5 AOD enhancement and CPL data

The CPL instrument on the ER-2 took profile measurements of the attenuated backscattering at 200m resolution down the centerline of each eMAS swath. This placement provided the opportunity to compare the two instruments to further quantify, characterize and validate the enhancements in AOD that are observed by eMAS near clouds. The centerline of eMAS was extracted by averaging the AOD pixels that fell within the CPL footprint. These indices could be used on all generated eMAS imagery. For CPL scenes not detected as “cloud”, extinction profiles were calculated from CPL backscattering profiles following Spinhirne et al., (1980, 1996). The lidar ratio is assumed to be constant and based on historical values for aerosol layer type. Aerosol layer typing is derived from geo-location, time-of-year, backscatter signal strength, depolarization ratio, and temperature. When integrated, the extinction profiles lead to AOD derived at 0.53 μm, comparable to eMAS-derived AOD at 0.55 μm.

Note that the CPL optical processing technique assumes a constant lidar ratio for the entire local scene, even though we might expect aerosol properties to change between background and near-cloud conditions, introducing an unquantifiable level of uncertainty in the CPL-derived AOD. For 9 September 2013 (Flight 13963 track #6), CPL assigned an aerosol type of polluted continental, with a lidar ratio of 59 sr. For the 30 August 2013 case (flight 13959 track #10), an aerosol type of a smoke/dust mixture was assigned, with a lidar ratio of 58 sr.

Figures 16 and 17 show the comparison between eMAS and CPL for the case studies of and 9 September (track #6) (Figs. 11-14) and 30 August (track #10) (Fig. 1), respectively. The black lines running down the centerline of the eMAS 0.5 km images represent cloud detection by the CPL instrument (at 200 m). The bottom graphs in each figure show collocated column AOD from each instrument. The CPL AOD, represented in red, included subpixel clouds that created spikes in the dataset, represented by transparent red in the figure. These spikes were removed by separating every 100 sequential measurements into sets, and eliminating the largest 15th percentile in each set.

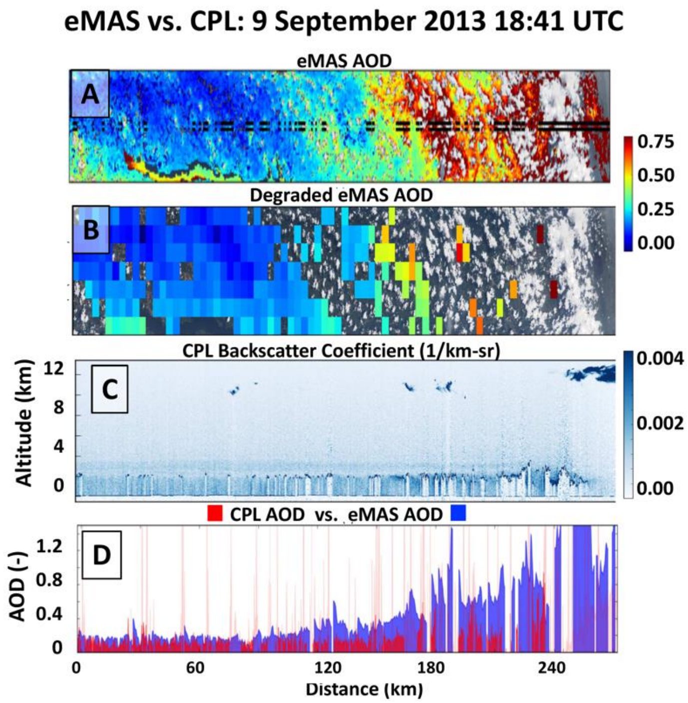

Figure 16: eMAS vs. CPL on 9 September 2013 at 1841 UTC (flight # 13963, Track #06).. (A) eMAS AOD (0.55 μm) at 0.5 km resolution superimposed onto the RGB image. (B) same but at 5 km resolution, (C) CPL attenuated total backscatter (0.53 μm) profile at 200m resolution. (D) eMAS AOD (0.55 μm) at 0.5 km in blue with CPL AOD (0.53 μm) at 200 m in red. Note that the last ~60 km in Fig. 11 has been truncated (thick cloud).

In Fig. 16, the reported AOD from the two instruments tend to agree in the left part of the image where there are fewer clouds. However, where cloudiness increases, beginning at roughly 100 km from the left edge, eMAS 0.5 km AOD becomes high relative to CPL AOD. The small amount of cirrus (>9 km in altitude) identified by CPL around 70 km does not appear to impact the eMAS AOD retrieval. CPL again identifies high cirrus around 175 km, 185 km and >250 km, but the eMAS high AOD appears independent of those clouds. Although only retrieving in the larger clear areas, the lower-resolution 5 km eMAS retrievals agree with the higher resolution even for high AOD.

In Fig. 17, the eMAS and CPL AODs track each other even better than in Fig. 16, with the eMAS AOD exhibiting a consistent high bias. There is no evidence of high cirrus cloud identified by CPL in this case, and the lower resolution eMAS retrieval does not pick up the high AOD between clouds.

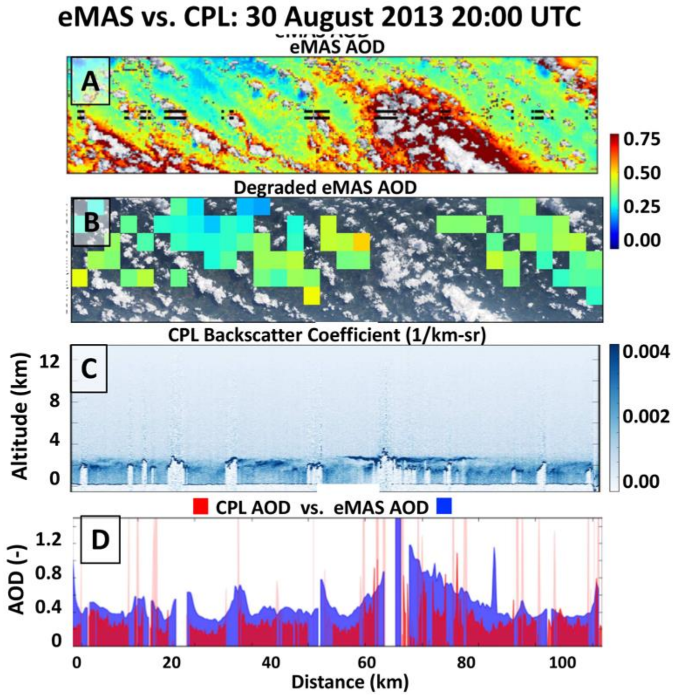

Figure 17: eMAS vs. CPL on 30 August 2013 at 2000 UTC (flight # 13959, Track #10). (A) eMAS AOD (0.55 μm) at 0.5 km resolution superimposed onto the RGB image. (B) same but at 5 km resolution, (C) CPL attenuated total backscatter (0.53 μm) profile at 200m resolution. (D) eMAS AOD (0.55 μm) at 0.5 km in blue with CPL AOD (0.53 μm) at 200 m in red.

The scatter plots in Fig. 18 attempt to quantify the AOD of each instrument as a function of cloud density. In the 9 September case (left), the CPL-derived AOD shows a slight correlation with cloud density ($r^2 = 0.34$), but this pales in comparison with the strong correlation shown by the eMAS-derived AOD ($r^2 = 0.86$). In the 30 August case (right), we again see strong correlation with eMAS-AOD (r^2=0.65), but fail to see any with the CPL product (i.e. $r^2 = 0.07$). Because CPL-derived AOD is only sensitive to physical changes to the aerosol particles such as hydration of aerosol near the cloud, the slight correlation between CPL-AOD and cloud density on 9 September suggests some AOD enhancements due to these physical changes are occurring. However, the eMAS AOD correlation to cloud density is so much stronger than the CPL-AOD correlation, most of the eMAS AOD enhancement near clouds must be due to effects not measured by CPL such as cloud adjacency effects. This suggests that these examples are situations where aerosol physical changes are not a significant factor and cloud adjacency effects provide the only explanation for enhancement. It is important to note that in each case however, that when cloud density approaches zero, both instruments converge to the same value, validating the clear sky retrievals of eMAS.

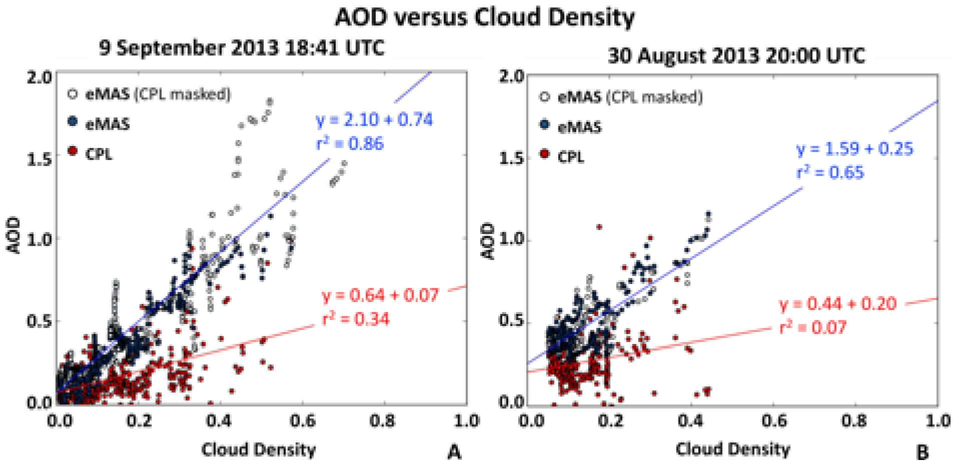

Figure 18: eMAS AOD (0.55 μm) in blue and CPL AOD (0.53 μm) in red plotted against cloud density for 9 September 2013 at 1841 UTC (A) and 30 August 2013 at 2000 UTC (B). Both instruments are in agreement in clear sky conditions (i.e. cloud fraction approaches 0.0) while eMAS shows much greater enhancement with higher cloud density. On 9 September there is some enhancement that is independent of the eMAS retrieval suggesting physical change to the particles in the vicinity of clouds, while on 30 August there is little or none.

Additionally, these effects are not limited to the two examples given. There are 27,990 data points if we plot AOD versus cloud density for all eMAS-CPL collocated retrievals in every scene that occurred during the 30 August, 6 September, and 9 September flights. Cloud density does not induce a significant effect in CPL AOD when generalizing across many scenes (i.e. r^2 = 0.03). However, eMAS AOD with respect to cloud density exhibits an overall stronger correlation (i.e. r^2 = 0.38). The much stronger relationship of eMAS AOD to cloud density when compared with CPL AOD, suggests that physical changes to aerosol particles in the transition zone plays less of a role than do cloud adjacency or 3-D effects in the overall enhancement of eMAS AOD near clouds. Varnai et al. (2013) comparing CALIPSO and MODIS retrievals in the vicinity of clouds found that the adjacency effect contributes significantly to near-cloud reflectance enhancements and is responsible to at least 30% of MODIS enhancement of AOD near clouds. More study is needed, however, including processing the remainder of the eMAS flight tracks at MODIS-like (and other) resolutions.

5 Summary and Conclusions

We successfully adapt the long-standing MODIS Dark Target (DT) aerosol algorithm to ingest measurements from the enhanced MODIS Airborne Simulator (eMAS), and retrieve aerosol products. We apply this ported algorithm to eMAS data collected during SEAC4RS that took place across the U.S. in August/September 2013. The advantage of eMAS is its ~50m spatial resolution, approximately 1/10 of the size of a MODIS pixel. We follow the structure of the DT algorithm, and retrieve aerosols at 0.5 km resolution. We also, for two cases, degrade the resolution (to 500 m) and retrieve at 5 km (more similar to a MODIS retrieval). With this new high-resolution data, we explore the complexity of retrieving aerosol information in the near cloud environment.

We compare the new 0.5 km eMAS retrievals to existing collocated MODIS observations by aggregating all eMAS retrievals that fell within a MODIS retrieval box when MODIS overpass fell within ±15 minutes of eMAS flight. Where both eMAS and MODIS report AOD, correlations are high ($r^2 \geq 0.61$), and eMAS tends to retrieve lower AOD than MODIS. In completely cloud-free conditions, the eMAS low offset is even more pronounced. This suggests that eMAS may be successfully masking out bright subpixels (such as urban surfaces or even tiny clouds) within the MODIS retrievals, and thus estimating the AOD "floor" within the scene. Then we look more closely at when each sensor produced a retrieval, and find it is more common to have an eMAS retrieval (but not MODIS), rather than a MODIS retrieval (but not eMAS). Since this is primarily because the finer resolution eMAS could be retrieving between clouds, we examine the histogram of eMAS AOD retrieval with and without concurrent retrieval. Overall, the mean eMAS AOD (~0.5) for when MODIS does not retrieve, is more than three times the AOD (0.14) for when MODIS also retrieves. The DT-retrieved AOD is significantly higher in cloud fields.

Next, we collocate eMAS AOD to AERONET observations, comparing mean eMAS AOD within a 6 km radius to AERONET AOD within ±30 minutes of overpass. Scatterplots indicate a high bias to eMAS AOD (regression slope of 1.85). However, within the local vicinity of the AERONET site (e.g. within 30 km or so), we find that eMAS reported much lower AOD which is more consistent with AERONET.

We explore whether the eMAS high AOD is due to cloud contamination (i.e., whether non-masked clouds are being retrieved as aerosol). When comparing the DT cloud mask that relies primarily on spatial variability versus the standard MODIS (MxD35-like) cloud mask, we find that the DT-aerosol cloud mask is more conservative, filtering out problematic surface features in addition to clouds. The conservative protective quality of the DT cloud mask employed during the eMAS aerosol retrieval is generally supported by the Cloud Physics Lidar (CPL) that observes the center of the eMAS track. One concern is that from the cases reported as cloudy by CPL, roughly 6% of the eMAS pixels were identified as clear and another 4% declared partly cloudy by the DT cloud mask. This suggests incomplete cirrus masking in the modified eMAS cloud masking, although comparison with CPL and eMASL2CLD ice retrievals does not confirm. Even if these cases might occur in 10% of the data, it does not appear that cloud contamination or undetected cirrus are the causes.

We explore the biased eMAS AOD using three quantifiable cloud parameters: distance to the nearest cloud, direction to the nearest cloud and cloud coverage/cloud density in the immediate area of the retrieval. Since the DT-aerosol cloud mask was also identifying non-clouds, we chose to use the MxD35-like cloud masks designations of cloudy or probably cloudy to determine the cloud parameters. There was some correlation between eMAS AOD and the distance to the nearest cloud, as well as some based on direction to cloud compared to direction of sun (e.g. sun-side and shadows). However, the strongest correlation occurred for a calculated "cloud density" parameter that accounted for the cloud field within 20 km of the retrieval. Cloud density calculated for two individual flight tracks accounted for nearly 80% of the AOD variance. Clearly, fine resolution AOD is enhanced when retrieved within cloud fields. Similar reports can be found throughout the literature for various resolution AOD products (e.g. Bar-Or et al., 2010; Varnai and Marshak, 2014).

One question is whether the enhancement is due to physical processes in the transition zone between clouds and aerosols or due to remote sensing artifacts from cloud adjacency effects. To test, we collocate eMAS AOD retrievals and CPL lidar observations, while also inverting the lidar profiles into AOD, assuming lidar ratios based on aerosol type assumptions that are held constant for each flight track. While lidar observations should be sensitive to physical processes in the transition zone such as new particle generation, cloud processing or hydrated aerosols, they should not be sensitive to cloud adjacency effects (scattering light to the satellite). We find that the lidar AOD has little to no relationship to cloud density in the overall SEAC4RS data set although there is a relationship for at least one flight line. Therefore, we conclude that the primary reason that eMAS AOD is offset high compared to both MODIS and AERONET values in these data is because of cloud adjacency effects.

This study is limited by its bounds to a few areas of the U.S. (mostly the Southeast) during a short season (late August and earlier September). It is also limited because we do not have directly collocated satellite (e.g. MODIS) retrievals to compare with. However, by exploring the retrievals at different resolutions, we better compare with MODIS sampling.

Further work can be done by applying the DT data products to other historical and future eMAS campaigns and summarizing them through similar analysis. Continued analysis is needed to explain the remaining bias and unexplained variance in variegated meteorological conditions in order to calibrate and validate the DT algorithm for these high-resolution retrievals. The enhancements to AOD that occur are likely dependent upon meteorological conditions, aerosol type and cloud properties, which were not explicitly studied in this work. Although, we note that meteorological conditions during SEAC^{4}RS favor shallow cumulus development and are the dominant cloud type in the individual case studies presented in this analysis.

Another limiting factor of this analysis is the lack of retrieved particle size information. Such information as Ångström exponent would help identify possible physical changes to particles in the vicinity of clouds (e.g., Varnai et al., 2017). Unfortunately, such information cannot be reliably retrieved from eMAS using the DT over land retrieval and thus was not included in this study. We need to add in-situ measurements and other observations to help tackle such problems (e.g., Jeong and Li, 2010)

As shown with degraded eMAS retrievals, the standard MODIS products are inadequate for studying the near-cloud environment and the effect on aerosol and aerosol remote sensing in that environment. This study demonstrates the value of high-spatial resolution AOD products to satisfy interest in the near-cloud environment. This not only means eMAS, but other high-resolution multi-spectral sensor such as Landsat (e.g., Barsi et al., 2016). All eMAS AOD data (at 0.5 km resolution) created within this study are available for users (eMASL2AER), and are easily compared to the already-processed cloud products (eMASL2CLD).

Acknowledgments, Samples, and Data

This eMAS data processing and analysis was primarily funded by NASA-ROSES, specifically the "NNH13ZDA001N-ACCDAM: Atmospheric Composition Campaign Data Analysis and Modeling" program managed by Hal Maring. Rob Spencer's efforts were, in part, supported by NASA GSFC's 2016 summer internship program, and some of his work satisfied requirements for his M.S. degree from the University of Texas-Austin. We are grateful for the AERONET team and AERONET site PIs for deploying and maintaining the sunphotometer network during SEAC^{4}RS. We also thank Paulo Veglio (U. Wisconsin) for providing match files that collocate eMAS pixels with the CPL ground track.

Users can access the eMAS L1B, Aerosol and Cloud data products from https://mas.arc.nasa.gov/data/deploy_html/seac4rs_home.html and Quicklook imagery from https://modis-images.gsfc.nasa.gov/SEAC4RS/emas/emas_seac4rs_L2_imagery.html.

Information about the MODIS aerosol product and downloading instructions are available here: https://modis.gsfc.nasa.gov/data/dataprod/mod04.php. DOI: Levy, R., Hsu, C., et al., 2015. MODIS Atmosphere L2 Aerosol Product. NASA MODIS Adaptive Processing System, Goddard Space Flight Center, USA:

http://dx.doi.org/10.5067/MODIS/MOD04_L2.006 (Terra)

http://dx.doi.org/10.5067/MODIS/MYD04_L2.006(Aqua)

References

Ackerman, S. A., Frey, R., Strabala, K. I., Liu, Y., Gumley, L., Baum, B. A., & Menzel, W. P. (2010). Discriminating clear-sky from cloud with MODIS: Algorithm Theoretical Basis Document (MOD35) (6 ed., pp. 1–118). Cooperative Institute for Meteorological Satellite Studies, University of Wisconsin-Madison.

Ackerman, S. A., Holz, R. E., Frey, R., Eloranta, E. W., Maddux, B. C., & McGill, M. (2008). Cloud Detection with MODIS. Part II: Validation. *Journal of Atmospheric and Oceanic Technology*, *25*(7), 1073–1086. http://doi.org/10.1175/2007JTECHA1053.1.

Ahmad, Z., & Fraser, R. S. (1982). An Iterative Radiative Transfer Code For Ocean-Atmosphere Systems. *Journal of Atmospheric Sciences*, *39*, 656–665. http://doi.org/10.1175/1520-0469(1982)039%3C0656:AIRTCF%3E2.0.CO;2.

Anderson, T. L., Charlson, R. J., Winker, D. M., Ogren, J. A. & Holmén, K. (2003). Mesoscale Variations of Tropospheric Aerosols, *Journal of Atmospheric Sciences*, 60(1), 119–136, http://doi.org/10.1175/1520-0469(2003)060<0119:MVOTA>2.0.CO;2.

Bar-Or, R. Z., Koren, I., & Altaratz, O. (2010). Estimating cloud field coverage using morphological analysis. *Environmental Research Letters*, *5*(1), 014022. http://doi.org/10.1088/1748-9326/5/1/014022.

Barsi, J., Lee, K., Kvaran, G., Markham, B., & Pedelty, J. (2014). The Spectral Response of the Landsat-8 Operational Land Imager. *Remote Sensing*, *6*(10), 10232–10251. http://doi.org/10.3390/rs61010232.

Baum, B. A., Yang, P., Heymsfield, A. J., Platnick, S., King, M. D., Hu, Y.-X., & Bedka, S. T. (2005). Bulk Scattering Properties for the Remote Sensing of Ice Clouds. Part II: Narrowband Models. *Journal of Applied Meteorology*, *44*(12), 1896–1911. http://doi.org/10.1175/JAM2309.1.

Boucher, O., Randall, D., Artaxo, P., Bretherton, C., Feingold, G., Forster, P. M., et al. (2013). Clouds and Aerosols. In T. F. Stocker, D. Qin, G. K. Plattner, M. Tignor, S. K. Allen, J. Boschung, et al. (Eds.), *Climate Change 2013: The Physical Science Basis; Contribution of Working Group I to the Fifth Assessment Report of the Intergovernmental Panel on Climate Change*. Cambridge University Press.

Carroll, M. L., DiMiceli, C. M., Townshend, J. R. G., Sohlberg, R. A., Elders, A. I., Devadiga, S., et al. (2016). Development of an operational land water mask for MODIS Collection 6, and influence on downstream data products. *International Journal of Digital Earth*, *10*(2), 207–218. http://doi.org/10.1080/17538947.2016.1232756.

Chand, D., Wood, R., Ghan, S. J., Wang, M., Ovchinnikov, M., Rasch, P. J., et al. (2012). Aerosol optical depth increase in partly cloudy conditions. *Journal of Geophysical Research-Atmospheres*, *117*(D), 17207. http://doi.org/10.1029/2012JD017894.

Charlson, R. J., Ackerman, A. S., Bender, F. A.-M., Anderson, T. L., & Liu, Z. (2007). On the climate forcing consequences of the albedo continuum between cloudy and clear air. *Tellus Series B-Chemical and Physical Meteorology*, *59*(4), 715–727. http://doi.org/10.1111/j.1600-0889.2007.00297.x.

Chew, B. N., Campbell, J. R., Reid, J. S., Giles, D. M., Welton, E. J., Salinas, S. V., & Liew, S. C. (2011). Tropical cirrus cloud contamination in sun photometer data. *Atmospheric Environment*, *45*(37), 6724–6731. http://doi.org/10.1016/j.atmosenv.2011.08.017.

Davis, S., Hlavka, D., Jensen, E., Rosenlof, K., Yang, Q., Schmidt, S., et al. (2010). In situ and lidar observations of tropopause subvisible cirrus clouds during TC4. *Journal of Geophysical Research*, *115*(9), 1282. http://doi.org/10.1029/2009JD013093.

Dessler, A. E., & Yang, P. (2003). The distribution of tropical thin cirrus clouds inferred from terra MODIS data. *Journal of Climate*, *16*(8), 1241–1247. http://doi.org/10.1175/1520-0442(2003)16<1241:TDOTTC>2.0.CO;2.

Eck, T. F., Holben, B. N., Reid, J. S., Arola, A., Ferrare, R. A., Hostetler, C. A., et al. (2014). Observations of rapid aerosol optical depth enhancements in the vicinity of polluted cumulus clouds. *Atmospheric Chemistry and Physics*, *14*(21), 11633–11656. http://doi.org/10.5194/acp-14-11633-2014.

Eck, T. F., Holben, B. N., Reid, J. S., Dubovik, O., Smirnov, A., O'Neill, N. T., et al. (1999). Wavelength dependence of the optical depth of biomass burning, urban, and desert dust aerosols. *Journal of Geophysical Research*, *104*(D24), 31333–31349. http://doi.org/10.1029/1999JD900923.

Frey, R. A., Ackerman, S. A., Liu, Y., Strabala, K. I., Zhang, H., Key, J. R., & Wang, X. (2008). Cloud Detection with MODIS. Part I: Improvements in the MODIS Cloud Mask for Collection 5. *Journal of Atmospheric and Oceanic Technology*, *25*(7), 1057–1072. http://doi.org/10.1175/2008JTECHA1052.1.

Gao, B., Yang, P., Han, W., Li, R., & Wiscombe, W. (2002a). An algorithm using visible and 1.38-mu m channels to retrieve cirrus cloud reflectances from aircraft and satellite data. *Ieee Transactions on Geoscience and Remote Sensing*, *40*(8), 1659–1668. http://doi.org/10.1109/TGRS.2002.802454.

Gao, B.-C., Kaufman, Y. J., Tanré, D., & Li, R.-R. (2002b). Distinguishing tropospheric aerosols from thin cirrus clouds for improved aerosol retrievals using the ratio of 1.38-μm and 1.24-μm channels. *Geophysical Research Letters*, *29*(18), 36–1–36–4. http://doi.org/10.1029/2002GL015475.

Gao, B.-C., Meyer, K., & Ping Yang. (2004). A new concept on remote sensing of cirrus optical depth and effective ice particle size using strong water vapor absorption channels near 1.38 and 1.88 /spl mu/m. *Geoscience and Remote Sensing, IEEE Transactions on*, *42*(9), 1891–1899. http://doi.org/10.1109/TGRS.2004.833778.

Gupta, P., Levy, R. C., Mattoo, S., Remer, L. A., & Munchak, L. A. (2016). A surface reflectance scheme for retrieving aerosol optical depth over urban surfaces in MODIS Dark Target retrieval algorithm. *Atmospheric Measurement Techniques*, *9*(7), 3293–3308. http://doi.org/10.5194/amt-9-3293-2016.

Holben, B. N., Eck, T. F., Slutsker, I., Tanre, D., Buis, J. P., Setzer, A., et al. (1998). AERONET - A federated instrument network and data archive for aerosol characterization. *Remote Sensing of Environment*, *66*(1), 1–16. http://doi.org/10.1016/S0034-4257(98)00031-5.

Holz, R. E., Platnick, S., Meyer, K., Vaughan, M., Heidinger, A., Yang, P., et al. (2016). Resolving ice cloud optical thickness biases between CALIOP and MODIS using infrared retrievals. *Atmospheric Chemistry and Physics*, *16*(8), 5075–5090. http://doi.org/10.5194/acp-16-5075-2016.

Hoppel, W. A., Frick, G. M., & Larson, R. E. (1986). Effect of nonprecipitating clouds on the aerosol size distribution in the marine boundary layer. *Geophysical Research Letters*, *13*(1), 125–128. http://doi.org/10.1029/GL013i002p00125.

Hsu, N. C., Jeong, M. J., Bettenhausen, C., Sayer, A. M., Hansell, R., Seftor, C. S., et al. (2013). Enhanced Deep Blue aerosol retrieval algorithm: The second generation. *Journal of Geophysical Research-Atmospheres*, *118*(16), 9296–9315. http://doi.org/10.1002/jgrd.50712.

Hutchison, K. D., Heidinger, A. K., Kopp, T. J., Iisager, B. D., & Frey, R. A. (2014). Comparisons between VIIRS cloud mask performance results from manually generated cloud masks of VIIRS imagery and CALIOP-VIIRS match-ups. *International Journal of Remote Sensing*, *35*(13), 4905–4922. http://doi.org/10.1080/01431161.2014.932465.

Ichoku, C., Chu, D. A., Mattoo, S., Kaufman, Y. J., Remer, L. A., Tanre, D., et al. (2002). A spatio-temporal approach for global validation and analysis of MODIS aerosol products. *Geophysical Research Letters*, *29*(12). http://doi.org/10.1029/2001GL013206.

Jeong, M.-J., & Li, Z. (2010). Separating real and apparent effects of cloud, humidity, and dynamics on aerosol optical thickness near cloud edges. *Journal of Geophysical Research: Atmospheres (1984–2012)*, *115*(D7). http://doi.org/10.1029/2009JD013547.

Karnieli, A., Kaufman, Y. J., Remer, L., & Wald, A. (2001). AFRI — aerosol free vegetation index. *Remote Sensing of Environment*, *77*(1), 10–21. http://doi.org/10.1016/S0034-4257(01)00190-0.

Kaufman, Y. J., Hobbs, P. V., Kirchhoff, V., Artaxo, P., Remer, L. A., Holben, B. N., et al. (1998). Smoke, Clouds, and Radiation - Brazil (SCAR-B) experiment. *Journal of Geophysical Research-Atmospheres*, *103*(D24), 31783–31808. http://doi.org/10.1029/98JD02281.

Kaufman, Y. J., Tanre, D., Remer, L. A., Vermote, E. F., Chu, A., & Holben, B. N. (1997). Operational remote sensing of tropospheric aerosol over land from EOS moderate resolution imaging spectroradiometer. *Journal of Geophysical Research*, *102*(D14), 17051–17067. http://doi.org/10.1029/96JD03988.

Kaufman, Y., Remer, L., Tanre, D., Li, R., Kleidman, R., Mattoo, S., et al. (2005). A critical examination of the residual cloud contamination and diurnal sampling effects on MODIS estimates of aerosol over ocean. *Ieee Transactions on Geoscience and Remote Sensing*, *43*(12), 2886–2897. http://doi.org/10.1109/TGRS.2005.858430.

Kim, H.-W., Yeom, J.-M., Shin, D., Choi, S., Han, K.-S., & Roujean, J.-L. (2017). An assessment of thin cloud detection by applying bidirectional reflectance distribution function model-based background surface reflectance using Geostationary Ocean Color Imager (GOCI): A case study for South Korea. *Journal of Geophysical Research-Atmospheres*, *122*(15), 8153–8172. http://doi.org/10.1002/2017JD026707.

King, M. D., Menzel, W. P., Grant, P. S., Myers, J. S., Arnold, G. T., Platnick, S. E., et al. (1996). Airborne Scanning Spectrometer for Remote Sensing of Cloud, Aerosol, Water Vapor, and Surface Properties. *Journal of Atmospheric and Oceanic Technology*, *13*(4), 777–794. http://doi.org/10.1175/1520-0426(1996)013<0777:ASSFRS>2.0.CO;2.

King, M. D., Platnick, S., Wind, G., Arnold, G. T., & Dominguez, R. T. (2010). Remote sensing of radiative and microphysical properties of clouds during TC4: Results from MAS, MASTER, MODIS, and MISR. *Journal of Geophysical Research: Atmospheres (1984–2012)*, *115*(D10), 11781. http://doi.org/10.1029/2009JD013277.

King, M. D., Platnick, S., Yang, P., Arnold, G. T., Gray, M. A., Riedi, J. C., et al. (2004). Remote sensing of liquid water and ice cloud optical thickness and effective radius in the Arctic: Application of airborne multispectral MAS data. *Journal of Atmospheric and Oceanic Technology*, *21*(6), 857–875. http://doi.org/10.1175/1520-0426(2004)021<0857:RSOLWA>2.0.CO;2.

Kittaka, C., Winker, D. M., Vaughan, M. A., Omar, A., & Remer, L. A. (2011). Intercomparison of column aerosol optical depths from CALIPSO and MODIS-Aqua. *Atmospheric Measurement Techniques*, *4*(2), 131–141. http://doi.org/10.5194/amt-4-131-2011.

Kopp, T. J., Thomas, W., Heidinger, A. K., Botambekov, D., Frey, R. A., Hutchison, K. D., et al. (2014). The VIIRS Cloud Mask: Progress in the first year of S-NPP toward a common cloud detection scheme. *Journal of Geophysical Research-Atmospheres*, *119*(5), 2441–2456. http://doi.org/10.1002/2013JD020458.

Koren, I., Feingold, G., Jiang, H., & Altaratz, O. (2009). Aerosol effects on the inter-cloud region of a small cumulus cloud field. *Geophysical Research Letters*, *36*, L14805. http://doi.org/10.1029/2009GL037424.

Koren, I., Remer, L. A., Kaufman, Y. J., Rudich, Y., & Martins, J. V. (2007). On the twilight zone between clouds and aerosols. *Geophysical Research Letters*, *34*(8), L08805. http://doi.org/10.1029/2007GL029253.

Levy, R. C., Mattoo, S., Munchak, L. A., Remer, L. A., Sayer, A. M., Patadia, F., & Hsu, N. C. (2013). The Collection 6 MODIS aerosol products over land and ocean. *Atmospheric Measurement Techniques*, *6*(11), 2989–3034. http://doi.org/10.5194/amt-6-2989-2013.

Levy, R. C., Munchak, L. A., Mattoo, S., Patadia, F., Remer, L. A., & Holz, R. E. (2015). Towards a long-term global aerosol optical depth record: applying a consistent aerosol retrieval algorithm to MODIS and VIIRS-observed reflectance. *Atmospheric Measurement Techniques*, *8*(10), 4083–4110. http://doi.org/10.5194/amt-8-4083-2015.

Levy, R. C., Remer, L. A., & Dubovik, O. (2007a). Global aerosol optical properties and application to Moderate Resolution Imaging Spectroradiometer aerosol retrieval over land. *Journal of Geophysical Research-Atmospheres*, *112*(D13), D13210. http://doi.org/10.1029/2006JD007815.

Levy, R. C., Remer, L. A., Mattoo, S., Vermote, E. F., & Kaufman, Y. J. (2007b). Second-generation operational algorithm: Retrieval of aerosol properties over land from inversion of Moderate Resolution Imaging Spectroradiometer spectral reflectance. *Journal of Geophysical Research: Atmospheres (1984–2012)*, *112*(D13), D13211. http://doi.org/10.1029/2006JD007811.

Li, R. R., Remer, L., Kaufman, Y. J., Mattoo, S., Gao, B. C., & Vermote, E. (2005). Snow and Ice Mask for the MODIS Aerosol Products. *Geoscience and Remote Sensing Letters*, *IEEE*, *2*(3), 306–310. http://doi.org/10.1109/LGRS.2005.847755.

Li, R.-R., Kaufman, Y. J., Gao, B.-C., & Davis, C. O. (2003). Remote sensing of suspended sediments and shallow coastal waters. *Geoscience and Remote Sensing*, *IEEE Transactions on*, *41*(3), 559–566. http://doi.org/10.1109/TGRS.2003.810227.

Mace, G. G., and Q. Zhang (2014). The CloudSat radar-lidar geometrical profile product (RL-GeoProf): Updates, improvements, and selected results, *J. Geophys. Res. Atmos.*, *119*, 9441–9462, http://doi.org/10.1002/2013JD021374.

Marquis, J. W., Bogdanoff, A. S., Campbell, J. R., Cummings, J. A., Westphal, D. L., Smith, N. J., & Zhang, J. (2017). Estimating Infrared Radiometric Satellite Sea Surface Temperature Retrieval Cold Biases in the Tropics due to Unscreened Optically Thin Cirrus Clouds.

Journal of Atmospheric and Oceanic Technology, *34*(2), 355–373. http://doi.org/10.1175/JTECH-D-15-0226.1.

Marshak, A., Evans, K. F., Várnai, T., & Wen, G. (2014). Extending 3D near-cloud corrections from shorter to longer wavelengths. *Journal of Quantitative Spectroscopy & Radiative Transfer*, *147*, 79–85. http://doi.org/10.1016/j.jqsrt.2014.05.022.

Marshak, A., Wen, G., Coakley, J. A., Remer, L. A., Loeb, N. G., & Cahalan, R. F. (2008). A simple model for the cloud adjacency effect and the apparent bluing of aerosols near clouds. *Journal of Geophysical Research: Atmospheres (1984–2012)*, *113*(D14), 83. http://doi.org/10.1029/2007JD009196.

Martins, J. V., Tanré, D., Remer, L., Kaufman, Y., Mattoo, S., & Levy, R. (2002). MODIS Cloud screening for remote sensing of aerosols over oceans using spatial variability. *Geophysical Research Letters*, *29*(12), 32,139. http://doi.org/10.1029/2001GL013252.

McGill, M., Hlavka, D., Hart, W., Scott, V. S., Spinhirne, J., & Schmid, B. (2002). Cloud Physics Lidar: instrument description and initial measurement results. *Applied Optics*, *41*(18), 3725–3734. http://doi.org/10.1364/AO.41.003725.

Meyer, K., & Platnick, S. (2010). Utilizing the MODIS 1.38 μm channel for cirrus cloud optical thickness retrievals: Algorithm and retrieval uncertainties. *Journal of Geophysical Research: Atmospheres (1984–2012)*, *115*(D24). http://doi.org/10.1029/2010JD014872.

Meyer, K., Platnick, S., Arnold, G. T., Holz, R. E., Veglio, P., Yorks, J., & Wang, C. (2016). Cirrus cloud optical and microphysical property retrievals from eMAS during SEAC⁴RS using bi-spectral reflectance measurements within the 1.88 μm water vapor absorption band. *Atmospheric Measurement Techniques*, *9*(4), 1743–1753. http://doi.org/10.5194/amt-9-1743-2016.

Muhlbauer, A., & Lohmann, U. (2009). Sensitivity Studies of Aerosol–Cloud Interactions in Mixed-Phase Orographic Precipitation. *Journal of Atmospheric Sciences*, *66*(9), 2517–2538. http://doi.org/10.1175/2009JAS3001.1.

Munchak, L. A., Levy, R. C., Mattoo, S., Remer, L. A., Holben, B. N., Schafer, J. S., et al. (2013). MODIS 3 km aerosol product: applications over land in an urban/suburban region. *Atmospheric Measurement Techniques*, *6*(7), 1747–1759. http://doi.org/10.5194/amt-6-1747-2013.

Patadia, F., Levy, R. C., & Mattoo, S. (2018). Correcting for trace gas absorption when retrieving aerosol optical depth from satellite observations of reflected shortwave radiation. *Atmospheric Measurement Techniques*, *11*(6), 3205–3219. http://doi.org/10.5194/amt-11-3205-2018.

Petrenko, M., Ichoku, C., & Leptoukh, G. (2012). Multi-sensor Aerosol Products Sampling System (MAPSS). *Atmospheric Measurement Techniques*, *5*(5), 913–926. http://doi.org/10.5194/amt-5-913-2012.

Pierce, J. R., Kahn, R. A., Davis, M. R., & Comstock, J. M. (2010). Detecting thin cirrus in Multiangle Imaging Spectroradiometer aerosol retrievals. *Journal of Geophysical Research: Atmospheres (1984–2012)*, *115*(D8). http://doi.org/10.1029/2009JD013019.

Platnick, S., Meyer, K. G., King, M. D., Wind, G., Amarasinghe, N., Marchant, B., et al. (2017). The MODIS Cloud Optical and Microphysical Products: Collection 6 Updates and Examples From Terra and Aqua. *Geoscience and Remote Sensing, IEEE Transactions on*, *55*(1), 502–525. http://doi.org/10.1109/TGRS.2016.2610522.

Quaas, J., Stevens, B., Stier, P., & Lohmann, U. (2010). Interpreting the cloud cover - aerosol optical depth relationship found in satellite data using a general circulation model.

Atmospheric Chemistry and Physics, *10*(13), 6129–6135. http://doi.org/10.5194/acp-10-6129-2010.

Remer, L. A., Kaufman, Y. J., Tanre, D., Mattoo, S., Chu, D. A., Martins, J. V., et al. (2005). The MODIS Aerosol Algorithm, Products, and Validation. *Journal of Atmospheric Sciences*, *62*(4), 947–973. http://doi.org/10.1175/JAS3385.1.

Remer, L. A., Mattoo, S., Levy, R. C., & Munchak, L. A. (2013). MODIS 3 km aerosol product: algorithm and global perspective. *Atmospheric Measurement Techniques*, *6*(7), 1829–1844. http://doi.org/10.5194/amt-6-1829-2013.

Remer, L. A., Mattoo, S., Levy, R. C., Heidinger, A., Pierce, R. B., & Chin, M. (2012). Retrieving aerosol in a cloudy environment: aerosol product availability as a function of spatial resolution. *Atmospheric Measurement Techniques*, *5*(7), 1823–1840. http://doi.org/10.5194/amt-5-1823-2012.

Rosenfeld, D., Sherwood, S., Wood, R., & Donner, L. (2014). Climate Effects of Aerosol-Cloud Interactions. *Science*, *343*(6169), 379–380. http://doi.org/10.1126/science.1247490.

Sassen, K. and Cho, B.S. (1992). Subvisual-Thin Cirrus Lidar Dataset for Satellite Verification and Climatological Research. Journal of Applied Meteorology, 31, 1275-1285. http://dx.doi.org/10.1175/1520-0450(1992)031<1275:STCLDF>2.0.CO;2.

Sayer, A. M., Hsu, N. C., Bettenhausen, C., & Jeong, M. J. (2013). Validation and uncertainty estimates for MODIS Collection 6 “Deep Blue” aerosol data. *Journal of Geophysical Research-Atmospheres*, *118*(14), 7864–7872. http://doi.org/10.1002/jgrd.50600.

Sayer, A. M., Munchak, L. A., Hsu, N. C., Levy, R. C., Bettenhausen, C., & Jeong, M. J. (2014). MODIS Collection 6 aerosol products: Comparison between Aqua's e-Deep Blue, Dark Target, and “merged” data sets, and usage recommendations. *Journal of Geophysical Research-Atmospheres*, *119*(24), 13,965–13,989. http://doi.org/10.1002/2014JD022453.

Seinfeld, J. H., Bretherton, C., Carslaw, K. S., Coe, H., DeMott, P. J., Dunlea, E. J., et al. (2016). Improving our fundamental understanding of the role of aerosol−cloud interactions in the climate system. *Pnas*, *113*(21), 5781–5790. http://doi.org/10.1073/pnas.1514043113.

Spinhirne, J. D., Hart, W. D., & Hlavka, D. L. (1996). Cirrus infrared parameters and shortwave reflectance relations from observations. *Journal of Atmospheric Sciences*, *53*(10), 1438–1458.

Spinhirne, J. D., Reagan, J. A., & Herman, B. M. (1980). Vertical-Distribution of Aerosol Extinction Cross-Section and Inference of Aerosol Imaginary Index in the Troposphere by Lidar Technique. *Journal of Applied Meteorology*, *19*(4), 426–438.

Stubenrauch, C. J., Rossow, W. B., Kinne, S., Ackerman, S., Cesana, G., Chepfer, H., et al. (2013). Assessment of Global Cloud Datasets from Satellites: Project and Database Initiated by the GEWEX Radiation Panel. *Bulletin of the American Meteorological Society*, *94*(7), 1031–1049. http://doi.org/10.1175/BAMS-D-12-00117.1

Su, W., Schuster, G. L., Loeb, N. G., Rogers, R. R., Ferrare, R. A., Hostetler, C. A., et al. (2008). Aerosol and cloud interaction observed from high spectral resolution lidar data. *Journal of Geophysical Research-Atmospheres*, *113*(D), 24202. http://doi.org/10.1029/2008JD010588

Tackett, J. L., & Di Girolamo, L. (2009). Enhanced aerosol backscatter adjacent to tropical trade wind clouds revealed by satellite-based lidar. *Geophysical Research Letters*, *36*(14). http://doi.org/10.1029/2009GL039264.

Tanre, D., Kaufman, Y. J., Herman, M., & Mattoo, S. (1997). Remote sensing of aerosol properties over oceans using the MODIS/EOS spectral radiances. *Journal of Geophysical*

Research: Atmospheres (1984–2012), *102*(D14), 16971–16988. http://doi.org/10.1029/96JD03437.

Tanre, D., Remer, L. A., Kaufman, Y. J., Mattoo, S., Hobbs, P. V., Livingston, J. M., et al. (1999). Retrieval of aerosol optical thickness and size distribution over ocean from the MODIS airborne simulator during TARFOX. *Journal of Geophysical Research: Atmospheres (1984–2012)*, *104*(D2), 2261–2278. http://doi.org/10.1029/1998JD200077.

Toon, O. B., Maring, H., Dibb, J., Ferrare, R., Jacob, D. J., Jensen, E. J., et al. (2016). Planning, implementation, and scientific goals of the Studies of Emissions and Atmospheric Composition, Clouds and Climate Coupling by Regional Surveys (SEAC4RS) field mission. *Journal of Geophysical Research-Atmospheres*, *121*(9), 4967–5009. http://doi.org/10.1002/2015JD024297.

Várnai, T., & Marshak, A. (2009). MODIS observations of enhanced clear sky reflectance near clouds. *Geophysical Research Letters*, *36*(6), 83. http://doi.org/10.1029/2008GL037089.

Várnai, T., & Marshak, A. (2012). Analysis of co-located MODIS and CALIPSO observations near clouds. *Atmospheric Measurement Techniques*, *5*(2), 389–396. http://doi.org/10.5194/amt-5-389-2012.

Várnai, T., & Marshak, A. (2018). Satellite Observations of Cloud-Related Variations in Aerosol Properties. *Atmosphere*, 1–17. http://doi.org/10.3390/atmos9110430.

Várnai, T., Marshak, A., & Eck, T. F. (2017). Observation-Based Study on Aerosol Optical Depth and Particle Size in Partly Cloudy Regions. *Journal of Geophysical Research-Atmospheres*, *122*(18), 10013–10024. http://doi.org/10.1002/2017JD027028.

Várnai, T., Marshak, A., & Yang, W. (2013). Multi-satellite aerosol observations in the vicinity of clouds. *Atmospheric Chemistry and Physics*, *13*(8), 3899–3908. http://doi.org/10.5194/acp-13-3899-2013.

Wang, T., Fetzer, E. J., Wong, S., Kahn, B. H., & Yue, Q. (2016). Validation of MODIS cloud mask and multilayer flag using CloudSat-CALIPSO cloud profiles and a cross-reference of their cloud classifications. *Journal of Geophysical Research-Atmospheres*, *121*(19). http://doi.org/10.1002/2016JD025239.

Wen, G., Marshak, A., Cahalan, R. F., Remer, L. A., & Kleidman, R. G. (2007). 3-D aerosol-cloud radiative interaction observed in collocated MODIS and ASTER images of cumulus cloud fields. *Journal of Geophysical Research*, *112*(D13), D13204. http://doi.org/10.1029/2006JD008267.

Wen, G., Marshak, A., Levy, R. C., Remer, L. A., Loeb, N. G., Várnai, T., & Cahalan, R. F. (2013). Improvement of MODIS aerosol retrievals near clouds. *Journal of Geophysical Research-Atmospheres*, *118*(16), 9168–9181. http://doi.org/10.1002/jgrd.50617

Wen, G., Marshak, A., Várnai, T., & Levy, R. (2016). Testing the two-layer model for correcting near-cloud reflectance enhancement using LES/SHDOM-simulated radiances. *Journal of Geophysical Research-Atmospheres*, *121*(16), 9661–9674. http://doi.org/10.1002/2016JD025021.

Zhang, J. & Reid, J. S. (2009). An analysis of clear sky and contextual biases using an operational over ocean MODIS aerosol product, *Geophysical Research Letters*, 36(15), https://doi.org/10.1029/2009GL038723.

Zhang, J., Reid, J. S., & Holben, B. N. (2005). An analysis of potential cloud artifacts in MODIS over ocean aerosol optical thickness products. *Geophysical Research Letters*, *32*(15), 32141. http://doi.org/10.1029/2005GL023254

Zhang, S., Wang, M., Ghan, S. J., Ding, A., Wang, H., Zhang, K., et al. (2016). On the characteristics of aerosol indirect effect based on dynamic regimes in global climate models. *Atmospheric Chemistry and Physics*, *16*(5), 2765–2783. http://doi.org/10.5194/acp-16-2765-2016.

Figure 19. Sample imagery of the DT algorithm applied to SEAC4RS eMAS flight track 13_959, Track #10 on 30 August 2013 20:00UTC. Plotted from left to right are (a) true-color RGB at 50 m, (b) DT-aerosol cloud mask at 50 m, and (c) the retrieved AOD (at 0.55 μm) at 0.5 km. Panels (d) and (e) are DT-cloud mask at 500 m and retrieved AOD at 5 km, corresponding to degraded eMAS resolution.

Figure 20. AOD (0.55 μm) from eMAS (Flight 13_955, Track #7, 17:59-18:11) superimposed on MODIS-Terra (3 km) observed at 17:40 UTC.

Figure 21. eMAS compared to MODIS AOD within ±30 minutes. (a) for 10 km MODIS data, and (b) for 3km MODIS data. Solid dots represent the mean of the eMAS AOD pixels compared to the value of encompassing MODIS AOD pixel; the error bars represent one standard deviation of the eMAS pixels. For each panel, the black line is the 1-1 line and the red line and equation represents the linear regression.

Figure 22. Spatiotemporal collocations of eMAS and MODIS pixels within 30 minutes of retrieval. eMAS pixels within a single MODIS (Aqua @ 3K) pixel are averaged and colored by their sample size. Sample size is proportional to the sample area resolution. In this case, sample size has a strong division, where small sample sizes of eMAS (cloudy) had a high bias and large sample sizes (clear sky) had a low bias, in comparison to MODIS. This separation exaggerates the low bias of eMAS and the potential effects of sub-pixel clouds

Figure 23. Categorical description to represent different combinations of eMAS vs MODIS retrieval success, along with (a) some possible reasons and (b) Frequency for each category, based on the MODIS 10 km product.

Figure 24. The eMAS AOD frequency distribution when there is success (green) or failure (blue) by MODIS ((a) = 10 km, (b) = 3 km)). Overall, there is a mean AOD enhancement of more than 0.34 (~220%) when eMAS retrieves within MODIS failed areas.

Figure 25. eMAS tracks and AERONET measurements collocated within a 6 km radius and a time window of +/- 30 min. The AERONET measurements are represented by the inner circles while the eMAS collocations are represented by the outer rings. This map shows only the collocations over the southeastern united states, but collocations that occurred in California were also accounted for in the analysis. The red box relates to the collocation described as Fig 9(f).

Figure 26. Scatter plot of collocated eMAS and AERONET AOD. Each point represents a spatial mean of eMAS retrievals within a 6 km radius of the AERONET station and a temporal mean of AERONET observations within +/- 30 minutes of eMAS overflight. The y-error bars are the standard deviation of the eMAS AOD pixels. The three regression lines are fit to all 57 points (black), to the 38 points which have larger eMAS sample size (red), and the 19 points with smaller sample size (blue).

Figure 27. Left, Panels (a)-(e): eMAS/AERONET AOD collocation (rings) superimposed on eMAS AOD. Inner rings are averaged AERONET AOD (±30 minutes) while outer ring is averaged eMAS AOD (6 km radius). eMAS Timestamps (track numbers) over AERONET site (lat, long) from left to right: (a): 9 September 20:37 UTC (Flight 13963 Track #11) over

Carthage site (32.06, -94.07); (b): 9 September, 22:19 UTC (Flight 13963 Track #16) over Baskin (32.28, -91.74); (c): 30 August, 19:17 UTC (Flight 13959 Track #07) over IMPROVE-MammothCave (37.13, -86.15); (d): 9 September, 20:52 UTC (Flight 13963 Track #12) over Leland_HS (33.40, -90.89); (e): 30 August, 17:59 UTC (Flight 13959 Track #03) over SEARCH_Centerville (32.90, -87.25). Right, (f) and (g): RGB (true-color) and AOD from the three-way collocation between eMAS/AERONET and MODIS 10 km retrieval, where the ring represents eMAS/AERONET collocation.

Figure 28. Comparison between DT and MxD35-like cloud masks for 30 August (a,b and c) and 6 September (d, e and f). Top, and middle panels are results from the MxD35-like and DT masks, respectively, where white color represents pixels identified as “cloud”. The bottom panels are the difference, where black shows difference (DT – MxD35-like). Almost every black pixel is the DT algorithm identifying more non-retrievable pixels than the MxD35 cloud mask.

Figure 29. eMAS aerosol and cloud retrievals from 9 September, 18:41 UTC (Flight 13963, Track #06), including (a) RGB and (b)1.88 μm reflectance, (c) Cloud Top Temperature, (d) Cloud phase, and (e) Ice cloud optical thickness, (f) the DT cloud mask and (g) retrieved AOD. Also plotted are calculations of the nearest cloud pixel in (h) and solar direction (i) of the nearest cloud using the cloud-products cloud mask (not shown). The AOD layer in (g) is superimposed onto the RGB image and includes AERONET (Calipso_Sabine_Frst and Calipso_Carthage sites) and CPL data. The AERONET measurements are represented by the inner circles while the eMAS collocations are represented by the outer circles. The CPL detection of clouds is represented by the two parallel lines that run down the centerline of (g). The white parallel lines in Panels (a) – (g) outline a small area characterized by thin ice cloud detection (above 1.88 μm threshold – blue line in (b) color bar) and retrieval.

Figure 30. Using the example flight track, retrieved eMAS AOD is compared to the distance to cloud. (a) Density histogram of all points within the image. Superimposed on this histogram are lines corresponding to the averaged AERONET (AOD=0.13±0.08, in green) and averaged eMAS (AOD=0.19, in red) collocated within 6 km of the two AERONET sites. Weighting the collocations to retrievals close-to-cloud yields AOD=0.24, whereas weighting to retrievals far-from-cloud yields AOD=0.13. (b) Similar to panel (a), but also separated by solar direction with respect to the sun (zenith angle of 27.45°) and the clouds (red-illuminated side; blue-shadow side). The lines are mean for each side, whereas shadings represent standard deviation. At 1 km from cloud, there is 0.08 difference between illuminated and shadowed cloud sides

Figure 31. Scatter plot of collocated eMAS and AERONET AOD, where the eMAS AOD is weighted toward its “background” level far from clouds and the AERONET value is temporal mean +/- 30 minutes of eMAS overflight.

Figure 32. An illustration for the density layer algorithm. Each eMAS retrieval (labeled as center pixel) takes on the weighted average of the MxD35-like cloud fractions for all retrieval boxes (labeled adjacent pixels) within 10 km from it. The red bounding box serves as the kernel that scans the entire cloud mask for clouds in the adjacent pixels and returns a cloud density value (between 0 and 1) in the active center pixel. Due to the boundary condition and the width of the kernel, the final density product is trimmed by 10km.

Figure 33. For 9 September, 18:41 UTC (Flight 13963, Track #06) eMAS AOD versus Cloud Density as derived from the MxD35-like cloud mask. (a): The scatter plot of all pixel values in the scene show the resulting relationship between cloud density and AOD using decay factor of b=8.0. (b): Modeled AOD image derived from the linear regression fitting presented in (a). (c): eMAS retrieved AOD at 0.55 μm.

Figure 34. eMAS vs. CPL on 9 September 2013 at 1841 UTC (flight # 13963, Track #06).. (a) eMAS AOD (0.55 μm) at 0.5 km resolution superimposed onto the RGB image. (b) same but at 5 km resolution, (c) CPL attenuated total backscatter (0.53 μm) profile at 200m resolution. (d) eMAS AOD (0.55 μm) at 0.5 km in blue with CPL AOD (0.53 μm) at 200 m in red. Note that the last ~60 km in Fig. 11 has been truncated (thick cloud).

Figure 35. eMAS vs. CPL on 30 August 2013 at 2000 UTC (flight # 13959, Track #10). (a) eMAS AOD (0.55 μm) at 0.5 km resolution superimposed onto the RGB image. (g) same but at 5 km resolution, (c) CPL attenuated total backscatter (0.53 μm) profile at 200m resolution. (d) eMAS AOD (0.55 μm) at 0.5 km in blue with CPL AOD (0.53 μm) at 200 m in red.

Figure 36. eMAS AOD (0.55 μm) in blue and CPL AOD (0.53 μm) in red plotted against cloud density for 9 September 2013 at 1841 UTC (A) and 30 August 2013 at 2000 UTC (b). Both instruments are in agreement in clear sky conditions (i.e. cloud fraction approaches 0.0) while eMAS shows much greater enhancement with higher cloud density. On 9 September there is some enhancement that is independent of the eMAS retrieval suggesting physical change to the particles in the vicinity of clouds, while on 30 August there is little or none.

Table 1. List of DT wavelength bands for MODIS and their MAS equivalents. Centroid wavelengths are listed for MODIS (second column), for eMAS during SEAC4RS (third column). *The MODIS 1.38 μm “cirrus” channel is replaced by 1.88 μm on MAS.